Article

Predictive Modelling of Land Cover Changes in the Greater Amanzule Peatlands Using Multi-Source Remote Sensing and Machine Learning Techniques

Alex Owusu Amoakoh [1,*], Paul Aplin [2], Pedro Rodríguez-Veiga [3,4], Cherith Moses [1], Carolina Peña Alonso [5], Joaquín A. Cortés [1], Irene Delgado-Fernandez [6], Stephen Kankam [7], Justice Camillus Mensah [7] and Daniel Doku Nii Nortey [7]

[1] Department of History, Geography and Social Sciences, Edge Hill University, Ormskirk L39 4QP, UK; mosesc@edgehill.ac.uk (C.M.); joaquin.cortes@edgehill.ac.uk (J.A.C.)
[2] Department of Geography, Mary Immaculate College, V94 VN26 Limerick, Ireland; paul.aplin@mic.ul.ie
[3] Sylvera Ltd., London N1 7SR, UK; pedro@sylvera.io
[4] School of Geography, Geology and the Environment, University of Leicester, Leicester LE1 7RH, UK
[5] Grupo de Geografía, Medio Ambiente y Tecnologías de la Información Geográfica, Instituto de Oceanografía y Cambio Global, Universidad de Las Palmas de Gran Canaria, 35214 Las Palmas, Spain; carolina.pena@ulpgc.es
[6] Earth Sciences Department, Faculty of Marine and Environmental Sciences (INMAR), University of Cadiz, 11001 Cadiz, Spain; irene.delgado@uca.es
[7] Hen Mpoano (Our Coast), Takoradi WS-289-9503, Ghana; skankam@henmpoano.org (S.K.); jmensah@henmpoano.org (J.C.M.); dnortey@henmpoano.org (D.D.N.N.)
* Correspondence: lexizamoako@yahoo.com

Abstract: The Greater Amanzule Peatlands (GAP) in Ghana is an important biodiversity hotspot facing increasing pressure from anthropogenic land-use activities driven by rapid agricultural plantation expansion, urbanisation, and the burgeoning oil and gas industry. Accurate measurement of how these pressures alter land cover over time, along with the projection of future changes, is crucial for sustainable management. This study aims to analyse these changes from 2010 to 2020 and predict future scenarios up to 2040 using multi-source remote sensing and machine learning techniques. Optical, radar, and topographical remote sensing data from Landsat-7, Landsat-8, ALOS/PALSAR, and Shuttle Radar Topography Mission derived digital elevation models (DEMs) were integrated to perform land cover change analysis using Random Forest (RF), while Cellular Automata Artificial Neural Networks (CA-ANNs) were employed for predictive modelling. The classification model achieved overall accuracies of 93% in 2010 and 94% in both 2015 and 2020, with weighted F1 scores of 80.0%, 75.8%, and 75.7%, respectively. Validation of the predictive model yielded a Kappa value of 0.70, with an overall accuracy rate of 80%, ensuring reliable spatial predictions of future land cover dynamics. Findings reveal a 12% expansion in peatland cover, equivalent to approximately 6570 ± 308.59 hectares, despite declines in specific peatland types. Concurrently, anthropogenic land uses have increased, evidenced by an 85% rise in rubber plantations (from $30,530 \pm 110.96$ hectares to $56,617 \pm 220.90$ hectares) and a 6% reduction in natural forest cover (5965 ± 353.72 hectares). Sparse vegetation, including smallholder farms, decreased by 35% from $45,064 \pm 163.79$ hectares to $29,424 \pm 114.81$ hectares. Projections for 2030 and 2040 indicate minimal changes based on current trends; however, they do not consider potential impacts from climate change, large-scale development projects, and demographic shifts, necessitating cautious interpretation. The results highlight areas of stability and vulnerability within the understudied GAP region, offering critical insights for developing targeted conservation strategies. Additionally, the methodological framework, which combines optical, radar, and topographical data with machine learning, provides a robust approach for accurate and detailed landscape-scale monitoring of tropical peatlands that is applicable to other regions facing similar environmental challenges.

1. Introduction

In an era characterised by the escalating ramifications of global climate change, including severe weather events and species extinction, the management of peatland emerges as a pivotal concern [1]. Peatlands are unique ecosystems formed in waterlogged environments where slow decomposition of plant material leads to the accumulation of peat, a dense organic matter [2]. Such accumulations, often extending over millennia, establish them as significant carbon sinks, playing an essential role in climate change mitigation efforts. Globally, they are estimated to hold 650 billion tonnes of carbon on 3% of the Earth's land surface, which is equivalent to more than half of the carbon in the atmosphere or the carbon stored by Earth's vegetation [1]. They also provide a wide range of ecosystem services including water purification, flood mitigation, biodiversity conservation, and the provision of a landscape with cultural, recreational, and livelihood values [3–5].

Despite their importance, peatlands face significant threats from anthropogenic land-use changes, including logging, agricultural expansion, plantation development, urban and industrial expansion, deforestation, drainage, and accidental burning [6–9]. These activities contribute to the destruction of approximately 500,000 hectares of peatlands annually [10,11]. The United Nations Environment Programme [6] reports that the current rate of loss and degradation of healthy peatland is ten times faster than the rate of expansion over the last 10,000 years. It is noted that around 12% of the estimated 500,000,000 ha of global peatlands are severely degraded to the extent that peat formation has ceased, leading to carbon stock losses [6]. Such land-use modifications decrease biodiversity and transform peatlands into net sources of greenhouse gases (GHGs), accelerating carbon dioxide emissions from drained peat soils [5]. They also trigger losses in hydrological integrity and peat subsidence, amplifying the risk of flooding and altering nutrient storage and cycling dynamics [12].

For the sustainable management of the remaining peatlands, enhancing our understanding of fundamental variables such as their spatial distribution, extent, changes over time, and future trends is crucial. However, significant uncertainties persist regarding these variables, particularly in tropical regions [13–15]. Historically, peatland research has been predominantly focused on boreal and temperate zones, leaving tropical peatlands comparatively underexplored [14,15]. Although the past two decades have seen a surge in tropical peatland studies, most have concentrated on Southeast Asia, which hosts an estimated 56% of tropical peatlands [4,16]. In contrast, African peatlands remain largely understudied, with uncertainties as to their extent, land cover dynamics, and future scenarios. For instance, the Congo Basin peatlands were recently estimated to cover approximately 14.55 million hectares and store around 30.6 billion tonnes of carbon [13]. Subsequent research revised their extent to 16.76 million hectares [17]. This significant adjustment confirms the uncertainties and knowledge gaps that exist, especially in Africa. In Ghana, the Greater Amanzule Peatlands (GAP) have been identified as a significant biodiversity hotspot experiencing rapid development due to agricultural plantation expansion, urbanisation, and the burgeoning oil and gas industry [18–21]. Since the onset of oil and gas activities in 2011, these pressures have intensified, threatening the peatland's ecological integrity and the ecosystem services it provides [19]. This underscores the urgent need for accurate land cover information and predictive modelling to inform effective management and conservation strategies for tropical peatlands like the GAP.

Methodologically, optical data from medium spatial resolution sensors such as Sentinel-2 (10 m multispectral imagery) and Landsat (30 m multispectral imagery) have been the primary and most effective tools for peatland change analysis (e.g., [6,8,22–24]), owing to their spectral detail and availability. However, this approach is constrained by frequent

cloud cover in tropical regions, which hampers consistent observation. Recent classification approaches increasingly favour the integration of data from multiple sensors for improved landscape characterisation (e.g., [25–29]), particularly the integration of radar data such as that of the Synthetic Aperture Radar (SAR), which can penetrate cloud cover and provide reliable data under all weather conditions. This complementarity of optical and radar data enhances the potential for fine-scale peatland mapping in equatorial zones where cloud cover is a persistent challenge.

In parallel, the development of free and open-source software packages and the availability of increased computational power have significantly facilitated image analysis. This, in turn, has expanded the application of machine learning (ML) algorithms in land cover change analysis [30]. ML algorithms, such as Random Forest (RF), Support Vector Machine (SVM), and Artificial Neural Networks (ANNs), offer robust classification capabilities, particularly in heterogeneous landscapes like tropical peatlands (e.g., [11,14,31–33]). By leveraging multi-source remote sensing data, these algorithms can capture subtle spectral and textural differences, enhancing land cover classification accuracy and supporting the prediction of future land-use scenarios.

Despite these advancements, few studies have applied these techniques to African peatlands, limiting the ability to monitor land cover changes over time and project future scenarios, both of which are crucial for informed conservation and land management decisions. The use of multi-source data fusion and machine learning in the study of African peatlands, such as the GAP, provides an opportunity to address these challenges and contribute to a better understanding of tropical peatland dynamics in under-researched regions. This study contributes to this emerging field by integrating data from multiple sensors with advanced machine learning models to analyse land cover changes and provide robust predictions of future land cover scenarios in the GAP. Specifically, we (1) utilise RF to classify and detect land cover changes in the GAP from 2010 to 2020 (including 2015 as a key observation point), using combined optical, radar, and digital elevation data, and (2) predict future land cover scenarios up to 2040 with Cellular Automata Artificial Neural Networks (CA-ANN). The year 2010 served as a baseline before the onset of oil and gas activities in GAP, which began in 2011 [19]. The year 2015 allowed for the observation of land cover changes five years into these activities, while 2020 provided insight into land cover alterations a decade later, particularly following the emergence of small-scale gold mining activities in 2016.

2. Methodology

2.1. Study Area

GAP is in the Western Region (WR) of Ghana (Figure 1a). It spans the Coastal savanna and Rainforest zones of Ghana (Figure 1a) and traverses the four coastal districts of Jomoro, Ellembele, Ahanta West, and Nzema East (Figure 1b). The terrain predominantly consists of swampy lowlands and slightly elevated areas, with heights ranging from 0 to 196 metres above sea level (Figure 2).

The peatland's hydrology is characterised by a network of small, interconnected watercourses and tributaries that flow into the three major river bodies in the area—Amanzule River, River Ankobra, and the Tano River (Figure 2)—ultimately discharging into the Gulf of Guinea [34]. The hydrological processes are influenced by tidal fluctuations, rainfall, and groundwater dynamics, which collectively contribute to the formation and maintenance of the peat deposits [35].

The climate of the GAP is tropical wet, with an average annual precipitation of approximately 1500 mm and relative humidity of 87.5% [35]. The area has two rainy seasons: a major rainy season from April to July, and a minor rainy season from September to November. The dry season occurs from December to March, with the Harmattan winds bringing cooler, drier air from the northeast. Mean annual temperatures range from 24 °C to 28 °C, with slight variations due to the influences of the Gulf of Guinea and the

various water bodies. These climatic variations may have implications for the hydrological processes and ecosystem dynamics, affecting the peatland's structure and function [34].

Biodiversity assessment within the area has identified 400 species, of which 41 are presently recognised as threatened according to the International Union for Conservation of Nature (IUCN) Red List criteria [36,37].

Figure 1. Study area map: (**a**) agro-ecological zones and the regional administrative boundaries of Ghana; (**b**) identified patchy peatlands and communities fringing them, as well as the district administrative boundaries in the GAP. Peatland information was obtained from Hen Mpoano's data repository and is based on participatory GIS and ground truthing approach. Basemap: Google Hybrid, Map data (© 2023 Google).
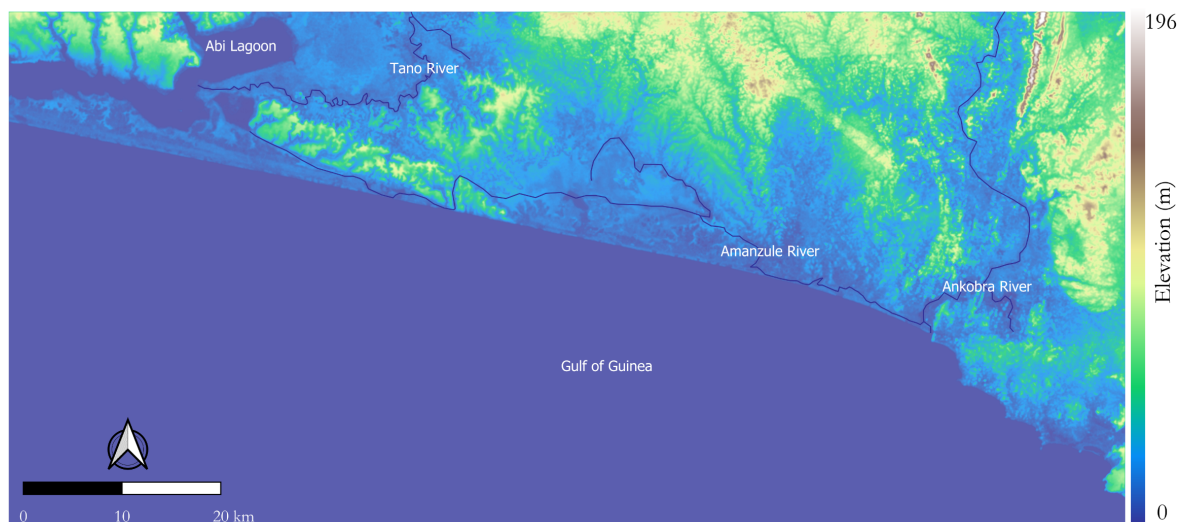

Figure 2. Digital elevation model (DEM) of the study area showing the Amanzule, Tano, and Ankobra rivers. The colour gradients represent variations in terrain elevation, with the scale indicating relative heights in meters above sea level (Source: authors' own creation using SRTM-derived DEM data accessed via Google Earth Engine).

2.2. Land Cover and Classification Scheme

Classifying tropical landscapes from remote sensing data is complex due to structural complexity, high heterogeneity, and the absence of a universal classification scheme for peatlands [14,15]. Therefore, defining appropriate thematic classes based on the characteristics of the study area and technical specifications of the imagery is important. A classification system was adopted based on extensive field observations of the study area and a careful study of relevant literature [6,15,38,39]. Peatland classes were adapted from the study of Lawson et al. [15], due to its detailed and comprehensive classification of peatland ecosys-

tems, which mirrors the diversity found within the study area. The adapted categories comprised mangrove swamp, mixed swamp, palm swamp, and bog plain; plantation comprised coconut, rubber, and oil palm; and artificial and bare classes included built-up land and bare surfaces, respectively. Other classes included sparse vegetation, natural forest, and water. In total, twelve classes were identified (Table 1).

Table 1. Land cover classification scheme based on Lawson et al. [15].

General Class	Land Cover Class	Class Description
Peatland	Mangrove swamp	Mangrove cover along coastal areas, predominantly composed of species such as *Rhizophora* and *Avicennia*
	Mixed swamp	Permanent and regularly flooded broadleaved trees and palm (Raphia sp.)
	Palm swamp	Permanent and regularly flooded areas of palm (predominantly Raphia sp.)
	Bog plain	Areas dominated by permanent and regularly flooded areas of grasses
Forest	Natural forest	Closed broadleaved evergreen forest with trees from medium to large sizes
Sparse	Sparse vegetation	Areas of sparse and/or stunted plant growth including other agricultural lands (i.e., young plantation trees, rainfed croplands)
Plantation	Coconut	Plantation of mature coconut trees
	Rubber	Plantation of mature rubber trees
	Oil palm	Plantation of mature oil palm trees
Artificial and bare areas	Built-up	Developed land such as buildings, asphalt roads and concrete surfaces, human settlements, and industrial facilities
	Bare surface	Areas of exposed soil or ground, open areas devoid of trees, grass, or other vegetation; often comprising land cleared for development
Hydrology	Water	Water bodies such as rivers, canals, lakes, and sea

2.3. Data

2.3.1. Satellite Imagery

A combination of optical, radar, and SRTM-derived DEM was used for the land cover classification (Table 2; Figure 3). This multi-source approach was adopted to enhance the accuracy of the land cover change analysis by leveraging the strengths of each data type [39]. All data were downloaded and processed using Google Earth Engine (GEE), a freely available machine learning and cloud computing platform capable of handling large datasets and having a comprehensive collection of preprocessed satellite imagery [40].

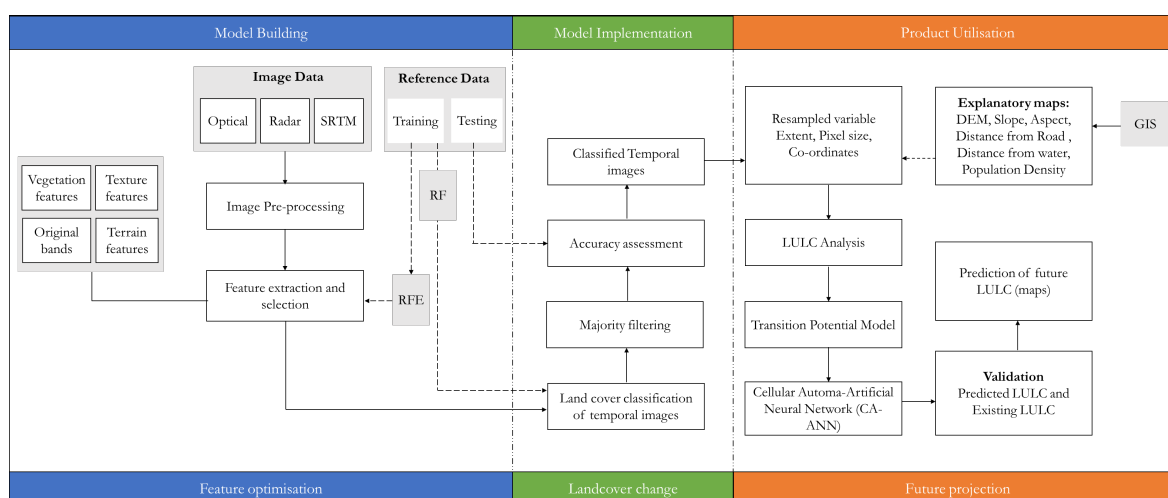
Figure 3. Workflow for land cover change analysis using multi-sensor data, featuring model building with Random Forest (RF) classification, feature optimisation through Recursive Feature Elimination (RFE), and GIS-based land cover projection.

Optical data were sourced from Landsat-7 and Landsat-8 Collection-1 Tier-1 calibrated top-of-atmosphere (TOA) reflectance products [40]. TOA data provided a more complete and consistent dataset across the time points of interest, ensuring broader temporal and spatial coverage. Given that this study focuses on land cover classification rather than direct spectral comparison over time, the use of TOA data was appropriate as each image was classified independently, reducing the impact of atmospheric correction on the classification outcomes. Additionally, the accuracy of each land cover map was rigorously assessed prior to conducting change detection analysis, ensuring the reliability of the final outputs.

ALOS/PALSAR and ALOS-2/PALSAR-2 satellites provided L-band Synthetic Aperture Radar (SAR) mosaic datasets [41]. SAR is important for its all-weather observation capability, especially relevant in the tropics where cloud cover can significantly hinder optical data acquisition. SAR's ability to penetrate cloud cover ensures the collection of consistent and reliable data across all seasons [41,42]. The SAR data had a spatial resolution of 25 m and included both horizontal transmit–horizontal receive (HH) and horizontal transmit–vertical receive (HV) polarisations [41]. To ensure the accuracy of the backscattering coefficient layers, JAXA has preprocessed them using their Sigma-SAR processor, which involved radiometric and geometric calibration, ortho-rectification, slope correction, co-registration, and intensity tuning of neighbouring strip data before ingesting into GEE [43]. This preprocessing step is also important for minimising errors and ensuring data consistency [41].

Additionally, terrain features from SRTM-derived DEM at 30 m resolution were incorporated as ancillary data to account for the influence of topography on land cover distribution. DEM data add valuable contextual information to the analysis, enabling a more comprehensive understanding of the factors driving land cover changes [44].

The Landsat and L-Band SAR images were acquired for the years 2010, 2015, and 2020, corresponding to a decade of land cover observation. These years were selected based on the availability of cloud-free remote sensing data, allowing for consistent and comparable analysis over time. The selected time frame provided an adequate temporal range for observing changes in land cover patterns.

Table 2. Satellite remote sensing data used for the land cover change analysis of the GAP.

Data Type	Satellite /Source	Description	Collection Periods	Advantages	Source
Multispectral optical	Landsat-7 and -8	TOA reflectance products	2010, 2015, 2020	Consistent coverage, enables detection of land cover changes over time [45,46]	U.S. geological survey
Synthetic aperture radar (SAR)	ALOS/ PALSAR and ALOS-2/PALSAR-2	L-Band SAR mosaic datasets	2010, 2015, 2020	Penetrates clouds, all-weather observations [41,42]	Japan Aerospace Exploration Agency (JAXA)
Digital elevation model (DEM)	SRTM-derived DEM	Elevation data	2000 (used as ancillary data)	Provides contextual information on topography [44]	U.S. geological survey

2.3.2. Reference Data

A combination of visual interpretation of very high-resolution imagery available in Google Earth Pro and field survey was employed to obtain the reference data. Prior information, including peatland inventory maps and pre-existing land cover classification [14,20,21,37], guided the establishment of strata [14], ensuring representative sampling across the varied landscape. To ensure accuracy, stakeholders who have extensive experience and familiarity with the landscape were involved in the visual interpretation process as their expertise contributed to a better understanding of the ground conditions. This

approach enhanced the representativeness of the reference data, accurately reflecting the different land cover types in the study area.

Reference data were represented as polygon features, which were then used to extract image pixels for training the classifier. This approach has been found to produce better classification outcomes than other methods, such as points (single pixels), point buffers (average pixel values), and image objects (area statistics) [47,48]. For the 2010, 2015, and 2020 image analyses, a total of 26,000, 25,700, and 30,000 image pixels were extracted as reference data, respectively. Of these reference data, 30% were randomly selected per class and set aside for testing. Image statistics were obtained based on the Landsat, L-Band SAR, and DEM image stack using the corresponding region of interest. Reflectance plots were constructed to visualise the distributions of reflectance per land cover type against each optical band (see Supplementary Figure S1). This approach ensured that the land cover classification scheme was grounded in both visual interpretation and quantitative analysis, leading to a more accurate and robust representation of the study area's land cover characteristics [49,50].

2.4. Preparation of Image Features

Annual composite images for the years 2010, 2015, and 2020 were generated from Landsat data using pixel-based compositing in Google Earth Engine (GEE). A median composite approach was employed to minimise the impact of outliers such as clouds and shadows, ensuring a representative depiction of surface conditions [27,45,51]. Pixel-based compositing also mitigated challenges such as insufficient data, pervasive cloud cover, disruptions in the image archive, atmospheric disturbances, and variations in radiometric readings due to seasonal transitions or changes in solar angles [52–54]. Cloud and shadow masking was performed using the CFMask algorithm to exclude affected pixels prior to applying the median filter. Given the persistent cloud cover in tropical regions, helper images from adjacent periods (±1 year) were utilised when insufficient cloud-free scenes resulted in data gaps for the target year [55,56]. In the case of 2010, Landsat-5 data from 2009 to 2011 were incorporated as helper data to address significant gaps caused by both cloud masking and the scan line corrector (SLC) failure in Landsat-7 imagery. To ensure the final image was consistent, we calibrated the reflectance values between Landsat-5 and Landsat-7 by applying a scaling process, ensuring that the combined data were radiometrically aligned and suitable for analysis. Temporal changes between consecutive years were assumed to be minimal, and the use of a median compositing method further mitigated potential inconsistencies. The number of scenes used per year varied between 53 and 65, ensuring adequate spatial and temporal coverage despite atmospheric conditions. For the radar data, the digital numbers (DN) were first converted to power-scaled intensity values. Subsequently, a Refined Lee filter was applied to each channel (HH, HV) to reduce speckle noise. These values were then converted to sigma–naught (σ^0) values, ensuring consistent and comparable backscatter values [41,57].

To ensure spatial resolution consistency across datasets, the radar data (25 m) were resampled to 30 m to align with the optical and DEM data. This was achieved using a bilinear interpolation method, which maintains the spatial characteristics of the radar data while aligning it with the optical data [58]. This approach helps to reduce potential errors or biases that could result from differing spatial resolutions [14,47].

After these preprocessing steps, we calculated a series of indices highlighting greenness, moisture, soil properties, and structural variations of the landscape to increase the utility of the spectral and radar information contained in the original image bands (Table 3). These indices are derived from the arithmetic combination of spectral reflectance measurements from Landsat imagery and backscatter coefficients from the SAR channels. Indices exhibit high correlation with vegetation characteristics such as phenology, biomass, moisture content, and leaf area index (LAI) [50,59], providing a comprehensive assessment of the ecological state of the landscape. To augment the analysis, texture features were extracted using the grey-level co-occurrence matrix (GLCM) from the SAR data. This texture analysis

focused on the radar backscatter to discern the structural variations within the landscape, offering insights into the physical arrangement and condition of the vegetation and other surface features. Texture metrics included contrast (CON), dissimilarity (DIS), inverse difference moment (IDM), angular second moment (ASM), mean (SAVG), correlation (COR), entropy (ENT), and variance (VAR). These metrics capitalise on SAR's unique ability to reflect the geometrical and structural properties of surface elements, enriching the land cover analysis with a level of detail unattainable through spectral data alone. The size of the neighbourhood included in each GLCM was set to 4, and the kernel size was 3×3 square using the '**glcmTexture**' function in GEE. The choice of kernel size followed literature in similar contexts [27,39,45].

Terrain features were generated from the SRTM-derived DEM data using the Terrain Analysis in Google Earth Engine (TAGEE) package [60]. The TAGEE package consists of a multi-band image containing the same data properties as the digital elevation model (resolution, data type, and coordinate reference system), with 13 bands (Table 3). Utilising all the terrain attributes of the package ensures a comprehensive analysis of the study area and provides the opportunity to test the relative importance of the features for tropical peatland (TP) delineation.

In total, 21 optical features, 28 radar features, and 13 terrain features served as input data in the machine learning model and analysis workflow (Table 3; Figure 3).

Table 3. Initial image features serving as potential predictors.

Datasets	Features	Description	Number of Features
Optical	Red, Green, Blue, NIR, SWIR1, SWIR2, GNDVI, MSAVI2, NDWI, EVI, NDVI, GEMI, ARVI, NBR, LSWI, VSSI, NBR2, NDSI, BI, SI, SAVI	Spectral bands and indices for vegetation (Normalised Difference Vegetation Index; Enhanced Vegetation Index; Green Normalised Difference Vegetation Index; Modified Soil-Adjusted Vegetation Index 2; Soil Adjusted Vegetation Index; Global Environmental Monitoring Index; Atmospherically Resistant Vegetation Index), water content (Normalised Difference Water Index; Land Surface Water Index), and soil and structural properties (Normalised Burn Ratio; Normalised Burn Ratio 2; Normalised Difference Salinity Index; Brightness Index; Salinity Index; Vegetation Soil Salinity Index), enhancing landscape characterisation.	21
Radar	HH_savg, HH_contrast, HV_contrast, HV_diss, HH_idm, HV_idm, HH_corr, HH_amp, HV_amp, HV_corr, HH_ent, HV_asm, HH_asm, HV_var, HH_diss, NDI, HV_stdDev, Diff, R1, R2, HV_savg, NLI, HH, HH_stdDev, HV, HH_var, HV_ent, Avg	Texture features from Synthetic Aperture Radar data (contrast, correlation, dissimilarity, entropy, angular second moment, variance, smoothed average—savg, standard deviation—stdDev, amplitude—amp) and indices (Normalised Difference Index—NDI; Average—Avg; Difference—Diff; Ratios—R1, R2; Normalised Lateral Index—NLI) to capture physical landscape variations, aiding in detailed land cover classification.	28
Terrain	Elevation, Eastness, Shape Index, Northness, slope, Hill shade, Gaussian Curvature, Mean Curvature, Vertical Curvature, Aspect, Horizontal Curvature, Minimal Curvature, Maximal Curvature	Topographic attributes from Shuttle Radar Topography Mission data, providing essential context for geomorphological analysis and land cover distribution.	13
Total number of features considered for the classification			62

2.5. Feature Selection and Classification

The image features (Table 3) were standardised by subtracting the mean and scaling to unit variance prior to classification. To deal with the challenge of overfitting, the recursive feature elimination (RFE) algorithm was used to reduce the number of features. RFE is a well-established iterative process that ranks and selects image features by eliminating the least important features based on stratified 2-fold cross-validation scores [61]. The algorithm creates a model with all the features, computes their importance scores, removes the least important features, and repeats the process until a desired subset of features is achieved. This process was employed via the Scikit-learn Python library [62], a widely used and robust library for machine learning applications. This was executed using Google Colab as the computational platform.

Identified important features were used to retrain a random forest (RF) algorithm for the classification. RF is an ensemble classifier that combines decision trees, bootstrap aggregation (bagging), and random subspace methods for classification and regression [63]. The combination of many weak learners in an ensemble contributes to RF achieving higher accuracy compared to machine learning algorithms based on a single classifier [63,64]. RF has become increasingly important in land cover classification in recent times because of its nonparametric nature, ability to limit overfitting, and its flexibility [32,49]. In their analysis of machine learning classifiers, Kaszta et al. [65] and Awuah et al. [47] also identified RF and SVM as the best performers among others that included k-nearest neighbours (kNN) and classification and regression trees (CART).

In the application of the RF classifier, two important parameters require careful selection to optimise the classifier's accuracy and computational efficiency: the number of trees (*ntree*) and the number of features considered for splitting at each node (*mtry*). The *ntree* and *mtry* were set at 100 and 2, respectively. This configuration is grounded in findings by Nomura et al. [27], who demonstrated that classification accuracy does not significantly increase beyond 100 trees in a similar study, noting that a higher number of trees contributes diminishing returns to model performance. Also, the *mtry* value of 2 enhances the diversity of the model by limiting the number of features considered for each split, thereby reducing the model's susceptibility to overfitting and improving its robustness.

Feature importance scores were also computed to determine the relative contribution of each image feature in the classification of the different land cover types. Some of the most frequent approximations for feature selection include Gini Index [66], gain-ratio [67], and Chi-square test [68]. Feature importance scores for the overall classification were estimated using the RF-based Gini criterion.

RF uses Gini Index for feature selection at each node [39,47]. When assigning an input pixel to a class (Ci), for a given training set (T), the Gini Index measures feature impurity with respect to the different classes and is expressed as

$$\sum \sum_{i \neq j} \left(\frac{f(C_i, T)}{(T|} \right) \left(\frac{f(C_j, T)}{(T|} \right), \tag{1}$$

where *f (Ci, T)* denotes the frequency of class *Ci* in the training set *T*, and *|T|* is the total number of elements in *T*. This formula iterates over all pairs of classes *i* and *j*, calculating the product of their relative frequencies and then summing these products to obtain the overall Gini Index. A lower Gini Index value indicates a higher purity of the node, contributing to more accurate classification outcomes in the RF model [47,69]. Feature importance scores for each land cover class were subsequently estimated from the product of the overall feature importance estimates and the standardised mean value of each feature split for the given class.

A post-classification majority filter was applied to improve class homogeneity using a 3 × 3 pixel moving window [27,39,49]. This approach examines and potentially modifies the classification of each pixel based on the prevailing class among its immediate eight neighbours. By aligning the class of a central pixel with the majority class found within its

surrounding context, this filtering technique effectively reduces the presence of isolated or anomalously classified pixels.

Accuracy of the classified images were evaluated using a confusion matrix [70], from which *precision*, *recall*, *F1 score*, *weighted F1 score*, and *Overall Accuracy* (OA) metrics were calculated using Equations (2)–(6). Accuracy-adjusted estimates of tropical peatland area coverage were obtained following Olofsson et al. [71].

$$Precision = \frac{tp}{tp + fp} \, , \tag{2}$$

$$Recall = \frac{tp}{tp + fn} \, , \tag{3}$$

$$F1 \ score = 2 \times \frac{Precision \times Recall}{Precision + Recall} \, , \tag{4}$$

$$F_1^{\text{weighted}} = \Sigma_{i=1}^{N} \left(\frac{S_i}{S_{\text{total}}} \times F_{1,i} \right) \, , \tag{5}$$

$$OA = \frac{tp + tn}{tp + fp + tn + fn} \, , \tag{6}$$

where *tp*, *fp*, *tn*, and *fn* represent the number of true positive, false positive, true negative, and false negative cases, respectively; S_i is the support (the number of true instances) for class *i*, S_{total} is the total support across all classes, and $F_{1,i}$ is the F1 score for class *i*.

2.6. Predicting Future Land-Use and Land Cover Changes with Cellular Automata and Artificial Neural Network (CA-ANN)

One aspect of this study was to predict land cover scenarios for the short term (2030) and long term (2040) using the CA-ANN model, which integrates Cellular Automata (CA) and Artificial Neural Networks (ANN). The CA model was selected for its capability to simulate complex spatial patterns of LULC changes [72–74], while ANN was incorporated to overcome CA's limitation in handling driving forces [74,75]. This model was implemented using the MOLUSCE plugin in QGIS, which involves steps including input data preparation, area change analysis, model calibration, simulation, and validation.

2.6.1. Model Input Data and Selection of Explanatory Variables

The first step in applying the CA-ANN model is to input historical LULC maps and associated explanatory maps, from which patterns will be studied to make future predictions. In this study, the historical maps used were the classified maps for 2010 and 2015. Explanatory maps are spatial variables hypothesised to influence the changes in the territory. It was hypothesised that terrain features (i.e., DEM, slope, and aspect), population density, proximity of resources to roads, and proximity of resources to water influence land cover change. The choice of explanatory parameters was based on a review of similar studies. For instance, Kamaraj and Rangarajan [76] reported that proximity to roads and water influence significant variations in land-use and land cover changes, often guiding the patterns of human settlement, agriculture, and resource exploitation. These variables serve as vital indicators that can delineate zones of varying vulnerability and propensity for change, thereby aiding in more accurate and predictive modelling of future land-use trajectories. Kamaraj and Rangarajan [76], and Kafy et al. [77], also noted that terrain features such as elevation, slope, and aspect influence land-use changes. The role of population density in shaping land-use dynamics is also crucial. Within this context,

distances related to roads and waterways were computed using vector representations of these features with the Euclidean distance function in ArcGIS software. The Euclidean distance measures the shortest path between two points in a plane or three-dimensional space using a straight line [78]. In two dimensions, the Euclidean distance between two points (x_1, y_1) and (x_2, y_2) is calculated as

$$\sqrt{(x_2 - x_1)^2 + (y_2 - y_1)^2} \, , \tag{7}$$

2.6.2. Quantifying Magnitude of LULC Changes and Transition Potential (Modelling)

The model was run on QGIS to analyse the input data, identifying locations where changes have occurred and quantifying the magnitude of these changes. This step is crucial for understanding the spatial and temporal dynamics of LULC changes within the study area. Following this, the CA-ANN model was employed for LULC change transition potential modelling, which aimed to determine all possible changes that occurred on the landscape. CA spatial filter was then applied to the transition potential maps to simulate future LULC scenarios. The parameter requirements for the model, such as the maximum iteration (500) and neighbourhood pixel size (3 × 3), were set based on studies conducted in similar contexts [76,77]. This choice of parameters ensures a reliable and accurate representation of LULC dynamics, considering the spatial complexity of the study area. Using the LULC data from 2010 and 2015, explanatory variables, and the transition matrices, LULC projections were generated for 2020, 2030, and 2040.

2.6.3. Model Validation

The reliability, functionality, and acceptance of the model were evaluated using the kappa coefficient, inherent to the MOLUSCE plugin in QGIS. The kappa coefficient is an established statistical parameter for quantifying the level of agreement between predicted and observed LULC maps, beyond what would be expected by chance [73,79,80]. The coefficient is calculated with the following formula:

$$Kappa\ (k) = \frac{P_o - P_e}{1 - P_e} \, , \tag{8}$$

where P_o represents the observed agreements and P_e is the expected agreement by chance. The observed agreement (P_o) is the sum of the probabilities of each category being correctly predicted:

$$P_o = \sum_{i=1}^{c} P_{ii} \, , \tag{9}$$

$$P_e = \sum_{i=1}^{c} (P_{i+} \times P_{+i}) \, , \tag{10}$$

P_{ii} denotes the probability of both raters agreeing on category i, P_{i+} is the sum of the probabilities across row i (the total predicted probability for category i), and P_{+i} is the sum of the probabilities down column i (the actual probability for category i). The subscript c denotes the number of categories.

The kappa value (k) ranges from -1 to 1, interpreting the agreement level: 0 indicates that the level of agreement is what would be expected purely by chance; a k value of 1 means there is complete agreement between the raters; conversely, a negative k value suggests that the agreement is worse than random chance, indicating a systematic disagreement between the raters.

3. Results

3.1. Feature Selection for Enhanced Land Cover Classification

After executing the RFE, the optimal number of features was obtained, as shown in Figure 4. This represents subsets of feature variables that combine to produce the best classification accuracy. The results show that out of the 62 features evaluated for the land cover classification, only 27 were deemed important for the classification process. Consequently, the highest accuracy for the dataset was achieved when these 27 features were employed. Beyond the optimal point (27, 0.9852), the accuracy score fluctuated as the number of features increased, indicating the presence of irrelevant or redundant features that did not enhance classification accuracy and necessitated removal.
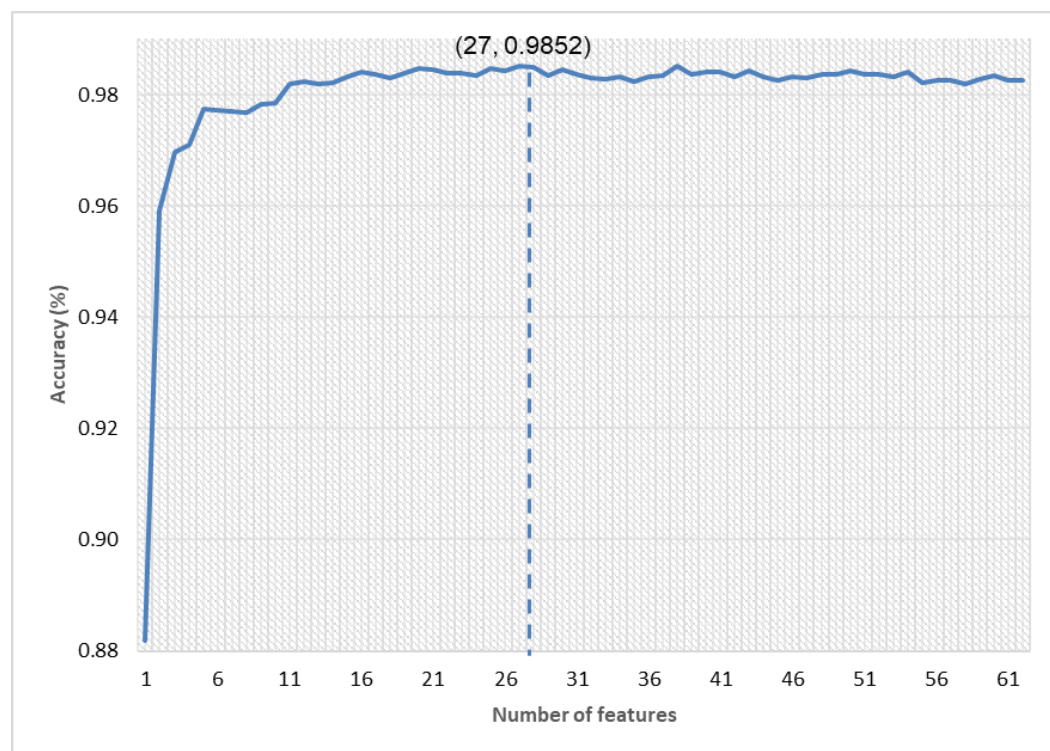

Figure 4. Plot of accuracy vs. number of image features.

The features retained for the classification included six original image bands (radar and optical), twelve spectral indices, four texture features, and five terrain features. Figure 5 shows the relative importance scores of the selected final input features in differentiating land cover categories. The top 10 most important features comprised five spectral indices, two original spectral bands, two terrain features, and one texture feature. Elevation emerged as the most important feature, followed by the texture feature HH_savg (Figure 5). Among the original spectral bands, SWIR1 displayed the highest importance, followed by SWIR2 and NIR. The most relevant spectral indices were SAVI, GNDVI, and MSAVI2, while the most influential terrain variables were elevation, slope, and Hill shade. Texture features with the highest importance were HH_savg, HV_savg, and NLI, respectively.

3.2. Classification Accuracy

The overall classification accuracy was high, achieving 93%, 94%, and 94% for the 2010, 2015, and 2020 classifications, respectively (Table 4). To provide a more comprehensive evaluation of the model's performance, weighted F1 scores were also calculated, yielding values of 0.80, 0.76, and 0.76 for 2010, 2015, and 2020, respectively. These scores account for class imbalances by weighting each class's F1 score based on its support, offering a balanced assessment of both precision and recall across all land cover types.
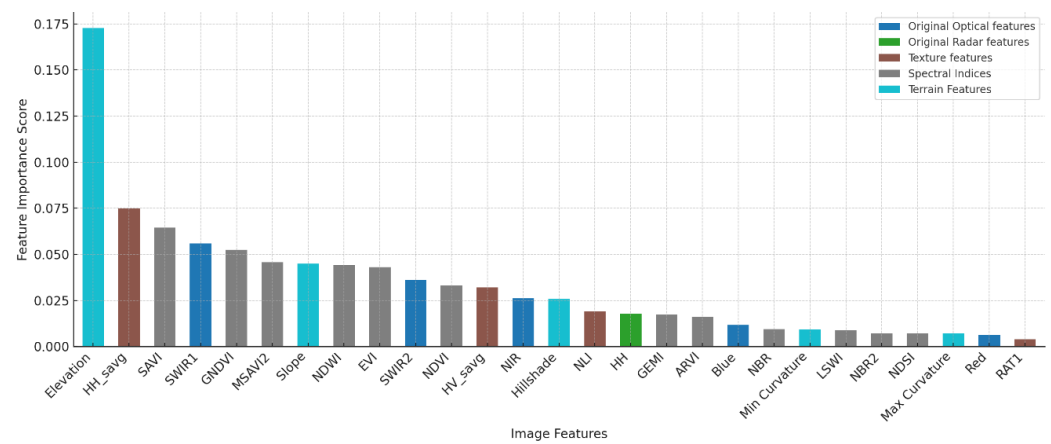
Figure 5. Feature importance scores of selected image features following RFE. Original bands, texture, spectral indices, and terrain features were chosen based on the number of features that retained optimal accuracy.

High accuracy was consistently observed in the Natural Forest category, with F1 score approaching 1, across all years, indicating robust classification performance. Mixed swamp and mangrove classes also showed improvement, particularly in F1 score metrics over time. In contrast, categories such as sparse vegetation and coconut exhibited lower F1 scores, highlighting areas where classification performance was less accurate and could benefit from further refinement. Consistent patterns of misclassifications were observed (see Supplementary Tables S1.1–S1.3). Notably, sparse vegetation was often misclassified with natural forests and rubber plantations across all maps. Bare surface and built-up areas were frequently confused in the 2015 and 2020 maps, while mangroves were occasionally misclassified as mixed swamp. Error matrices for each classification are presented in Supplementary Tables S1.1–S1.3.

Table 4. Model precision, recall, F1 score, OA, and weighted F1 score metrics of GAP for individual land cover categories and overall classification. Metrics are presented for each land cover class in the 2010, 2015, and 2020 datasets.

General Classes	Land Cover Classes	2010			2015			2020		
		Precision	Recall	F1 Score	Precision	Recall	F1 Score	Precision	Recall	F1 Score
Peatland	Mangrove	0.91	0.59	0.72	0.68	0.36	0.47	0.70	0.74	0.72
	Mixed swamp	0.97	0.93	0.95	0.95	0.92	0.94	0.97	0.90	0.93
	Palm swamp	0.75	0.75	0.75	0.77	0.75	0.76	0.80	0.69	0.74
	Bog plain	0.95	0.74	0.83	0.75	0.90	0.82	0.81	0.76	0.78
	Natural forest	0.95	0.97	0.96	0.94	0.99	0.97	0.94	0.99	0.97
	Sparse vegetation	0.18	0.24	0.20	0.37	0.41	0.39	0.38	0.50	0.43
Plantation	Rubber	0.89	0.96	0.93	0.93	0.77	0.84	0.68	0.48	0.57
	Coconut	0.49	0.55	0.52	0.40	0.47	0.43	0.28	0.54	0.37
	Oil palm	0.83	0.51	0.63	0.13	0.67	0.21	0.38	1	0.55
Artificial surface	Built-up	0.86	0.99	0.92	0.99	0.88	0.93	0.99	0.90	0.95
	Bare surface	1	0.75	0.86	1	0.50	0.67	1	0.75	0.86
	Water	0.99	0.99	0.99	1	1	1	1	1	1
Weighted F1 Score				0.80			0.76			0.76
OA		93%			94%			94%		

3.3. Land Cover Changes

The study observed extensive land cover changes between 2010 and 2020 (Figure 6). A total of 114,028 ha, accounting for 21% of the entire GAP, experienced change from 2010 to 2015. A similar extent of change was observed from 2015 to 2020, affecting another 113,014 ha (21% of the area). When areas classified as water bodies are excluded from this analysis, the proportion of GAP that underwent land cover transitions—either through reduction or expansion of particular cover types—increases to approximately 44% for 2010–2015 and 43% for 2015–2020. This recalibration serves to highlight the extent of terrestrial changes more clearly and offers valuable insights into the dynamics of human impacts on the landscape.
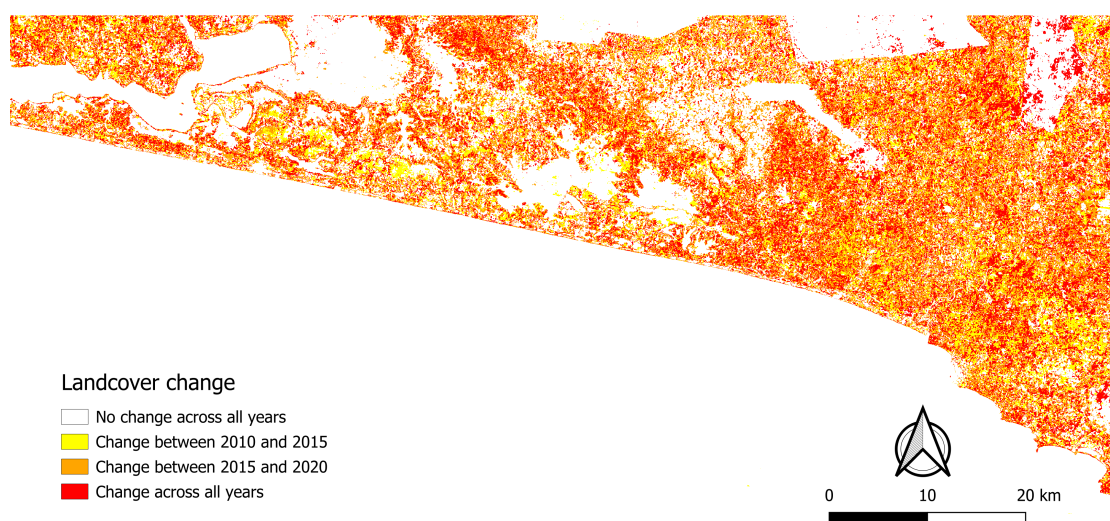

Figure 6. Land cover changes in the GAP between 2010, 2015, and 2020.

The spatial distribution of land cover and patterns of change across 2010, 2015, and 2020 are shown in Figure 7, while Table 5 presents land cover class areas and their respective changes throughout the study period. Although palm swamp forest experienced a substantial decline from 9647.91 ± 35.07 ha in 2010 to 6325 ± 24.68 ha in 2020, peatlands in general increased from $54,502 \pm 198.10$ ha in 2010 to $61,072 \pm 238.29$ ha in 2020 (Table 5). Mangrove initially contracted by 297.05 ± 7.91 ha between 2010 and 2015, before expanding by 209.21 ± 7.93 ha between 2015 and 2020. Bog plain also expanded moderately, from 1881.89 ± 6.84 ha in 2010 to 2410.98 ± 9.41 ha in 2020.

Sparse vegetation experienced a significant reduction from $45,064 \pm 163.79$ ha in 2010 to $29,424 \pm 114.81$ ha in 2020. On the other hand, rubber plantations experienced considerable growth (85%), increasing from $30,530 \pm 110.96$ ha in 2010 to $56,617 \pm 220.90$ ha in 2020. Coconut and oil palm plantations diminished in extent across the three time periods (Table 5).

Artificial surface exhibited steady growth from 4584 ± 16.66 ha in 2010 to 4946 ± 17.98 ha in 2015 to 5252 ± 20.49 ha in 2020. These findings underscore the dynamic nature of land cover changes in the GAP and highlight the importance of monitoring and understanding the driving forces behind these changes for better land-use planning and sustainable development.
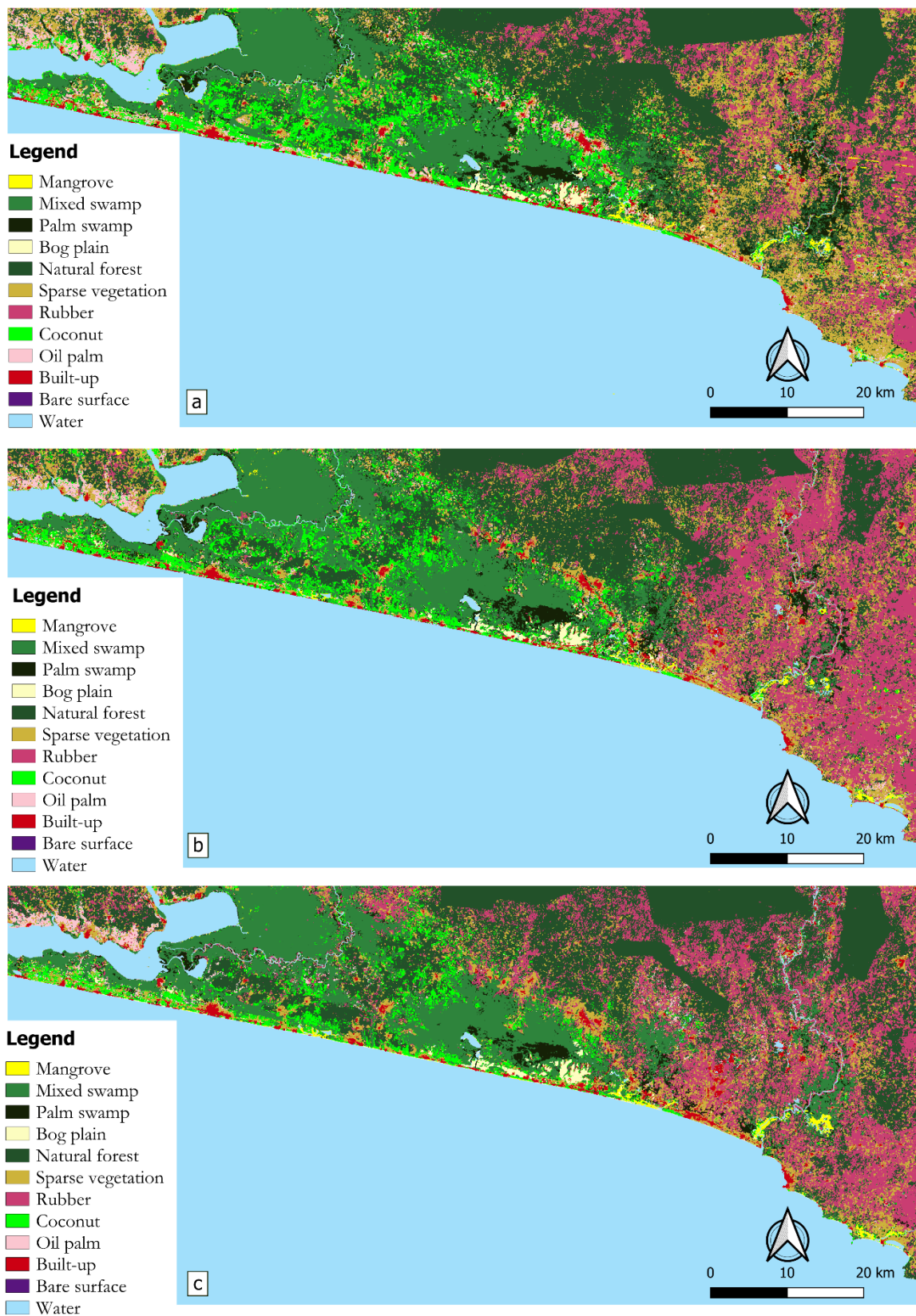
Figure 7. Land cover maps for GAP from (**a**) 2010, (**b**) 2015, and (**c**) 2020.

Table 5. Accuracy-adjusted land cover area and changes. Area of change corresponds to the proportion of the total area. (−) denotes area decrease of the land cover type. See Table 1 for the definitions of land cover types.

Land Cover Type	2010	2015	2020	2015/2010 Change (ha)	2020/2015 Change (ha)	2020/2010 Change (ha)
Mangrove	1687.31 ± 6.13	1390.26 ± 5.05	1599.47 ± 6.24	−297.05 ± 7.91	209.21 ± 7.93	−87.84 ± 8.76
Mixed swamp	41,285.57 ± 150.06	46,643.83 ± 169.53	50,736.49 ± 197.96	5358.26 ± 226.30	4092.66 ± 260.01	9450.92 ± 245.71
Palm swamp	9647.91 ± 35.07	8046.48 ± 29.25	6326.00 ± 24.68	−1601.43 ± 45.50	−1720.48 ± 38.20	−3321.91 ± 42.82
Bog plains	1881.89 ± 6.84	1892.77 ± 6.88	2410.98 ± 9.41	10.88 ± 9.74	518.21 ± 11.53	529.09 ± 11.64
Peatland	54,502.68 ± 198.10	57,973.34 ± 210.71	61,072.94 ± 238.29	3470.66 ± 289.38	3099.6 ± 317.45	6570.26 ± 308.59
Natural forest	96,623.40 ± 351.19	81,683.75 ± 296.89	90,658.03 ± 353.72	−14,939.65 ± 458.76	8974.28 ± 461.82	−5965.37 ± 497.73
Sparse vegetation	45,064.16 ± 163.79	31,119.10 ± 113.11	29,424.84 ± 114.81	−13,945.06 ± 195.82	−1694.26 ± 161.04	−15,639.32 ± 196.85
Rubber	30,530.00 ± 110.96	61,438.56 ± 223.31	56,617.24 ± 220.90	30,908.56 ± 237.78	−4821.32 ± 313.80	26,087.24 ± 235.21
Coconut	20,919.19 ± 76.03	18,183.26 ± 66.09	12,538.92 ± 48.92	−2735.93 ± 100.85	−5644.34 ± 81.76	−8380.27 ± 88.77
Oil-palm	9016.27 ± 32.77	5788.27 ± 21.04	5128.89 ± 20.01	−3228 ± 38.06	−659.38 ± 29.07	−3887.38 ± 37.41
Plantation	60,465.47 ± 219.77	85,410.08 ± 310.43	74,285.05 ± 289.84	24,944.61 ± 375.09	−11,125.03 ± 424.68	13,819.58 ± 361.39
Built-up	4560.93 ± 16.58	4920.67 ± 17.88	5207.28 ± 20.32	359.74 ± 24.40	286.61 ± 27.00	646.35 ± 26.22
Bare surface	23.45 ± 0.09	25.68 ± 0.09	45.57 ± 0.18	2.23 ± 0.13	19.89 ± 0.19	22.12 ± 0.19
Artificial surface	4584.38 ± 16.66	4946.35 ± 17.98	5252.85 ± 20.49	361.97 ± 24.48	306.5 ± 27.15	668.47 ± 26.33
Water	286,131.70 ± 1039.98	286,239.20 ± 1118.52	286,678.10 ± 1118.52	107.5 ± 1527.81	438.9 ± 1595.56	546.4 ± 1521.88

3.4. Relative Land Cover Transitions

Examination of the land cover transitions shows a landscape characterised by dynamic shifts (Figure 8). Establishment of rubber plantations primarily occur at the expense of forested areas, especially natural forest. Although there is evidence of peat swamp forest being converted to rubber (i.e., 4751.8 ha overall between 2010 and 2020), a more prominent trend of natural forest to rubber conversion is observed (i.e., 20,786.23 ha in the 2010–2015 period alone) (Supplementary Tables S2.1 and 2.2).

The results also suggest that palm swamps act as pioneer habitats in the ecological succession towards mixed swamps by colonising the landscape before other tree species become established to form a mixed-species swamp (mixed-swamp). This succession is reflected in the observed decrease in palm swamp areas (3149 ha from 2010 to 2015 and 2920 ha from 2015 to 2020) and a corresponding increase in mixed swamp areas (Supplementary Tables S2.1 and 2.2).

An observed agricultural shift highlights a transition from areas characterised by sparse vegetation (including smallholder food crop farms) and coconut plantations, towards rubber cultivation (Figure 8). About 27,091 ha of sparse vegetation cover transitioned to rubber from 2010 to 2020, with an additional 1482 ha moving from coconut to rubber within the same period. This shift likely reflects farmers' and landowners' responses to economic incentives, adjusting their crop choices to maximise financial returns.

Urban expansion was gradual, with built-up areas increasing by 360 ha (7.89%) from 4,561 ha in 2010 to 4921 ha in 2015, followed by a further increase of 286.28 ha (5.82%) between 2015 and 2020, culminating in a total of 5207.28 ha. A considerable amount of this urban development occurred on lands previously classified as sparse vegetation (Supplementary Tables S2.1 and 2.2).

3.5. Projected Land Cover Changes

GAP is projected to remain largely stable, with minor modifications expected for 2030 and 2040 (Table 6). Modest expansion is forecasted for mangrove and mixed swamp areas, with each expected to increase by 0.73 ha by 2030. This positive trend may be attributed to conservation efforts by non-governmental organisations and their donor partners (Hen Mpoano, 2016a, 2017 [20,21]). Palm swamp and natural forest areas are anticipated to exhibit minor declines of 0.09 ha and 0.18 ha, respectively (Table 6), indicative of ongoing habitat loss and fragmentation due to agricultural expansion, logging, and infrastructure development.

Rubber plantations and built-up areas are projected to expand modestly, with a projected increase of 1.57 ha and 15.25 ha, respectively (Table 6). This expansion reflects the growing demand for agricultural commodities and the need for urban development to support increasing human populations [81,82]. Conversely, coconut plantations, bog plains, and sparse vegetation areas are projected to contract marginally, with a decrease of 4.28 ha, 4.45 ha, and 8.94 ha, respectively (Table 6). Projecting further to 2040, mangrove, mixed swamp, palm swamp, rubber, oil palm, and built-up areas are expected to display net increases of 4.90 ha, 34.42 ha, 6.60 ha, 2.79 ha, 13.55 ha, and 23.53 ha, respectively (Table 6). These trends suggest that pressures driving land cover changes, such as agricultural expansion and urbanisation, are expected to persist. On the other hand, natural forest, sparse vegetation, coconut, and bog plains are expected to manifest net decreases of 11.59 ha, 10.42 ha, 4.66 ha, and 13.47 ha, respectively (Table 6). This indicates that the loss and degradation of these ecosystems may continue, with potential adverse consequences for biodiversity, ecosystem services, and local livelihoods.
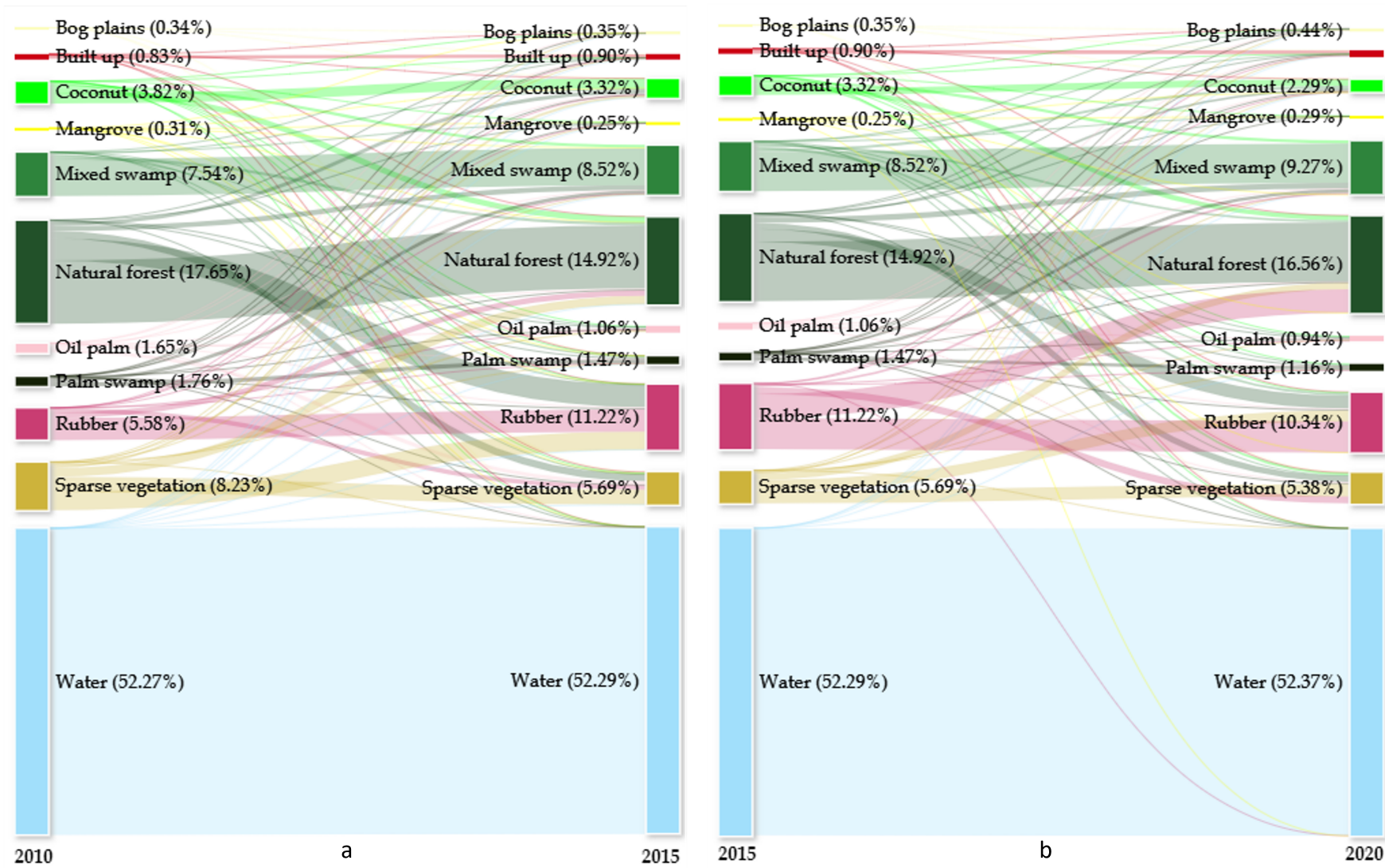
Figure 8. Sankey diagram showing dynamic land cover transitions in the GAP: (**a**) represents transitions from 2010 to 2015 and (**b**) depicts changes from 2015 to 2020.

Table 6. CA-ANN projections for land cover areas (in hectares) and their changes from 2020 to 2040. It details the forecasted land cover class areas for 2030 and 2040, and it quantifies the shifts in land cover from 2020 to 2030 and again from 2020 to 2040.

Land Cover	2030	2020–2030 Change	2040	2020–2040 Change
Mangrove	1600.20	0.73	1604.37	4.90
Mixed swamp	50,737.23	0.73	50,770.91	34.42
Palm swamp	6325.91	−0.09	6332.60	6.60
Bog plains	2406.53	−4.45	2397.51	−13.47
Natural forest	90,657.85	−0.18	90,646.43	−11.59
Sparse vegetation	29,415.90	−8.94	29,414.42	−10.42
Rubber	56,618.81	1.57	56,620.03	2.79
Coconut	12,534.64	−4.28	12,534.27	−4.66
Oil-palm	5128.89	0.00	5142.45	13.55
Built-up	5222.53	15.25	5230.81	23.53
Bare surface	45.57	0.00	46.35	0.78
Water	286,677.76	−0.36	286,631.66	−46.46

3.6. Evaluation of the CA-ANN Model for Land Cover Simulation

The overall Kappa value obtained for the CA-ANN model validation was 0.70, indicating a substantial agreement between the observed and simulated 2020 land cover maps. The accuracy rate was 80%, reflecting the percentage of land cover pixels that the model correctly classified when compared to the actual observed data during the validation process. The Kappa histogram (Category-Specific Kappa) value was 0.96, demonstrating an exceptionally high degree of consistency across different land cover categories. The kappa location value was 0.72, indicating a good level of spatial accuracy in matching the locations of observed and simulated land cover classes.

These results demonstrate the effectiveness of the CA-ANN model in accurately simulating land cover changes in the study area. However, it is important to note that the accuracy of the CA-ANN model may be influenced by various factors, including the quality of the input data, the choice of model parameters, and the complexity of the underlying land cover dynamics [83]. Therefore, future research should continue to refine and improve the model, as well as explore the use of alternative modelling approaches and data sources, to enhance the accuracy and robustness of land cover simulations [84].

4. Discussion of Results

4.1. Optimal Features for the Enhanced Land Cover Classification

The results showed that out of the 62 image features initially evaluated for the assessment, only 27 were considered essential for the classification process (Figure 4). These 27 features included six original image bands (radar and optical), twelve spectral indices, four texture features, and five terrain features, representing a diverse set of information that captures the unique spectral, spatial, and terrain characteristics of the land cover types in the study area.

The feature importance assessment identified elevation as the most important element for the land cover classification (Figure 5). This is consistent with our earlier findings [39], reinforcing the important role of terrain data in tropical peatland classification. Terrain characteristics offer insights into the physical and environmental factors affecting land cover distribution and are key in identifying the suitability of specific area's activities such as agriculture, infrastructure development, and conservation initiatives [60,82,85–87]. The radar-derived texture feature HH_savg was the second most important image feature in the classification, confirming the advantage of multi-source remote sensing data. This approach can be particularly effective for capturing the complex spatial heterogeneity of land cover types and offer a valuable solution in regions prone to cloud cover or where high-quality optical imagery is scarce [28,88].

Among the original spectral bands, the SWIR1 band exhibited the highest importance, followed by the SWIR2 and NIR bands (Figure 5). These findings align with research that have highlighted the enhanced sensitivity of SWIR and NIR bands in discriminating vegetation structures, moisture content, and land cover transitions [50,59,89,90]. Their wavelengths are adept at capturing distinct spectral signatures associated with different biophysical properties and land surface conditions [32].

The most relevant spectral indices included the SAVI, GNDVI, and MSAVI2, which are known to provide robust measures of vegetation condition and stress as well as minimise the influence of soil background and atmospheric effects [47,85,91]. The high importance scores of these indices confirm their effectiveness in differentiating between land cover types characterised by varying levels of vegetation cover and density, such as forests, plantations, and bogs [92–94].

Texture features with the highest importance were HH_savg, HV_savg, and NLI, respectively. According to Haralick et al. [95], texture features derived from the spatial arrangement and variability of pixel values within a given window can effectively capture the structural and contextual information of land cover types and improve the classification accuracy, especially for classes with similar spectral characteristics but distinct spatial patterns. The inclusion of these texture features in the optimal subset of image variables demonstrates their utility in enhancing the discriminative power of the classifier and the robustness of the land cover classification process [26,29,96].

4.2. Classification Accuracy

Many remote sensing studies typically employ surface reflectance to mitigate atmospheric effects (e.g., [25,33,52,97,98]); however, in this study, TOA reflectance was utilised, allowing for the acquisition of a greater number of cloud-free observations. Despite the potential uncertainties associated with TOA reflectance, the results demonstrated satisfactory classification performance, with high overall accuracies achieved across all land cover maps (Table 4). This can be attributed to the optimal selection of image features, the robustness of the random forest classifier, and the meticulous digitisation process that ensured the accuracy of reference data used for validation [48,70,71,99].

The satisfactory classification performance of individual land cover classes further confirms the effectiveness of the proposed methodology in capturing the spatial and spectral variability of different land cover types in the GAP. In particular, the peatland classes—including mangroves, mixed swamps, palm swamps, and bog plains—achieved F1 scores exceeding 0.7 in most cases, except for mangroves, which displayed lower accuracies due to their misclassification with mixed swamps (Table 4). This may result from the spectral similarity between these two classes (see Supplementary Figure S1), as well as their spatial proximity and the presence of mixed patches of mangroves and swamps in transitional zones [100,101]. However, the overall classification performance of peatland classes can still be considered satisfactory, considering the complexity and heterogeneity of these ecosystems and their susceptibility to various anthropogenic and natural disturbances that may alter their spectral characteristics [102,103].

Consistent patterns of misclassifications were identified among the other vegetation types (Supplementary Tables S1.1–S1.3). For example, the term 'sparse vegetation' encompassed a range of vegetation within the study area, such as young plantation trees, rainfed croplands, and small-scale agriculture (Table 1). Consequently, misclassifications of sparse vegetation and other land cover types were expected. Also, newly established rubber plantations, characterised by land cleared of most trees and woody vegetation but possibly retaining some trees for shade or a herbaceous understory, could be easily mistaken for sparse vegetation.

Misclassifications observed in the 2020 land cover map between rubber plantations and natural forests (Supplementary Table S1.3) may be attributed to the similarities in spectral reflectance and the spatial configuration of these classes such as the growth of mature rubber plantation crowns and improper planting spacing [104]. Bare surfaces and

built-up areas may also be misclassified due to the similar spectral appearance of dry soil and light-impervious surfaces such as concrete [105,106].

Overall, while lower accuracy metrics were observed for certain non-peatland classes (Table 4), we retained them in the classification schema due to their ecological importance and relevance to the study area's land-use patterns. Merging these classes would have risked oversimplifying the landscape, and the decision to keep them offers a more detailed representation of the spatial and ecological heterogeneity of the GAP.

4.3. Land Cover Changes

The spatial distribution of land cover and patterns of change across the three time periods revealed several notable trends and dynamics. For instance, the peatland classes, particularly mixed swamp and bog plains, exhibited expansion trends, whereas palm swamp forests showed a significant decline (Table 5). These changes may be related to various factors such as climate variability, hydrological alterations, natural processes, and anthropogenic pressures, including land-use changes [107–109]. Mangroves expanded from 2015 to 2020 and could be attributed to the successful implementation of conservation and mangrove restoration efforts by NGOs and local communities in the region since 2015 (Figure 9; [20,21]).

Figure 9. Early growth stages of replanted mangroves in GAP (Source: Hen Mpoano, [20]).

Bog plain expansions may be linked to natural processes such as peat formation and accumulation [85,110]. Conversely, reductions in sparse vegetation areas (encompassing a diverse range of land cover types such as young plantation trees, rainfed croplands, and small-scale agriculture; Table 1) may be attributed to the corresponding expansion of rubber plantations and urbanisation (Figure 7; Table 5). Rubber plantations experienced 85% growth, increasing from 30,530 ± 110.96 ha in 2010 to 56,617 ± 220.90 ha in 2020 (Table 5). This can be linked to the increasing global demand for natural rubber and favourable market conditions, which have incentivised land conversion to rubber plantations [111–113].

Declines in coconut and oil palm plantations may be related to factors such as disease outbreaks, changes in agricultural policies, or shifts in market preferences [114–118].

Built-up and bare areas exhibited steady growth from 2010 to 2020 (Figure 7; Table 5), reflecting the urbanisation and development in the GAP. This urban expansion may be driven by increasing population and reported infrastructural developments, particularly due to the expanding oil and gas activities in the region [20,34,35,119]. Conversion of lands for urban purposes can lead to habitat loss, fragmentation, and alterations in ecosystem functions, which in turn can have significant implications for biodiversity, ecosystem services, and human well-being [6,120].

The relative stability of water areas throughout the study period (Table 5) suggests that hydrological processes, such as surface runoff and evapotranspiration, have remained relatively constant over time [121]. However, further research is needed to investigate potential changes in water quality, groundwater resources, and aquatic ecosystems in response to land cover changes and human activities in the region.

These land cover changes highlight the complex interplay between natural processes, socioeconomic drivers, and policy interventions that shape land-use and land cover patterns over time. Understanding these dynamics is important for informing land-use planning, resource management, and conservation efforts aimed at promoting sustainable development and enhancing ecosystem resilience in the face of global environmental change [108,122,123].

4.4. Relative Land Cover Transitions

The assessment of land cover transitions within the GAP indicates significant shifts, with both losses and gains among various land cover types (Figure 8; Supplementary Tables S2.1 and S2.2). Establishment of rubber plantations was predominantly at the expense of natural forest and sparse vegetations (including smallholder food crop farms). This trend reflects broader patterns of deforestation for monoculture expansion in tropical regions [111–113,124,125], raising concerns about the long-term ecological sustainability of GAP and its capacity to support diverse ecosystems. Monoculture plantations can lead to soil nutrient depletion, increased pest pressures, and greater vulnerability to diseases [111]. It could also have significant implications for local livelihoods and food security by reducing the availability of land for food production and potentially disrupt traditional land-use systems [112].

Expansion of built-up and bare areas, collectively referred to as artificial surfaces, also occurred predominantly in areas previously occupied by sparse vegetation (Supplementary Tables S2.1 and S2.2). This confirms the ongoing urbanisation and infrastructure development within the GAP. Such changes can lead to reduced agricultural land availability, displacement of natural habitats, and potential disruption of local biodiversity and water cycles [112,126].

The results further suggest that palm swamps act as pioneer habitats in the ecological succession towards mixed swamps, initially colonising the landscape before other tree species become established to form a mixed-species swamp (Supplementary Tables S2.1 and S2.2). This transition is likely influenced by factors such as hydrology and natural succession processes [15], with the establishment of mixed swamp forests potentially offering increased habitat diversity and ecosystem functionality [1]. Such transitions underscore the dynamic nature of peatland ecosystems in the GAP.

In general, these land cover transitions have important implications for land management and conservation efforts. The conversion of natural forests to rubber plantations highlights the need for policies that balance agricultural expansion with the conservation of natural ecosystems. This may include the promotion of sustainable land management practices, such as agroforestry, which can enhance biodiversity and maintain ecosystem services while also supporting rural livelihoods [85,127,128]. Protecting and restoring palm swamp and mixed swamp ecosystems can also provide a valuable habitat for many species and contribute to the overall ecological integrity of the GAP. Conservation efforts should

focus on preventing further degradation and fragmentation of these ecosystems, as well as promoting the recovery of degraded areas through reforestation or assisted natural regeneration [6,129].

The expansion of built-up and bare surface areas indicates that urban planning and infrastructure development should be integrated with biodiversity conservation objectives. This may involve implementing land-use zoning and green infrastructure strategies that minimise habitat fragmentation and enhance ecological connectivity [19]. It is also important to continuously monitor and analyse land cover changes to inform land management and conservation decision-making. Remote sensing and GIS can be a valuable tool in this process, as demonstrated in this study, enabling stakeholders to better understand the drivers and consequences of these changes and to develop more effective strategies for sustainable land use and conservation [53,130].

4.5. Projected Land Cover Changes

Projections of land cover changes within the GAP for 2030 and 2040 were based on land cover transitions observed between 2010 and 2020, terrain characteristics, infrastructure proximity, and population density metrics. The results estimate minor changes in GAP (Table 6), implying that the ecological and developmental dynamics within the area are likely to maintain a steady state, with conservation efforts and development pressures achieving a delicate balance. However, these projections do not account for several factors that are likely to influence the land cover trajectory of the region. Notably absent are the effects of climate change, the implications of proposed mining concessions, the potential impacts of the proposed USD 60 billion petroleum hub project, the region's rapid population growth, and the absence of frequent temporal data points [20,21,119,131]. The omission of these drivers presents a limitation, as their potential to alter land cover and ecosystem dynamics could be significant. For instance, the lack of frequent temporal data points limits the model's capacity to capture short-term fluctuations and rapid transitions in this highly dynamic ecosystem.

Future studies should address these limitations by incorporating climate change scenarios, which are essential for understanding potential impacts on ecosystems, agriculture, and water resources. It is also crucial to include the land cover implications of large-scale projects such as the petroleum hub and mining activities, alongside population growth trends and other socioeconomic dynamics, to provide a more accurate and comprehensive forecast of land cover changes. Increasing the temporal resolution of the data by incorporating more frequent time points, such as annual data or even real-time data streams, would further enhance the ability to capture rapid transitions and short-term fluctuations. This approach would provide a more nuanced understanding of seasonal variations and smaller-scale disturbances, offering a more detailed and accurate representation of land cover dynamics. Additionally, evaluating the model's sensitivity to various parameters and assessing its robustness under different environmental scenarios will be valuable. Sensitivity analyses can identify which factors most significantly impact model outputs, guiding improvements in model structure and data collection priorities. By addressing these aspects, future research can significantly advance the predictive capabilities of our model, ensuring more reliable and actionable forecasts.

This initial projection should be viewed as an important baseline from which to gauge the potential impacts of the unconsidered factors, identify areas of both stability and vulnerability within the GAP, and inform targeted conservation and development strategies. Integrating these overlooked aspects will allow for a better understanding of the dynamic interplay between natural processes and human activities, facilitating the development of nuanced strategies that ensure the sustainability and resilience of GAP's land cover. By doing so, policymakers, conservationists, and stakeholders can undertake informed actions that balance ecological preservation with socioeconomic development, ensuring the long-term well-being of the region and its inhabitants.

4.6. Contrasting Projections with Existing Literature

This study projects a net increase in mangrove areas, a decrease in natural forest cover, and a modest expansion of rubber plantations and built-up areas by 2040. Such projections contrast with global trends of mangrove degradation and diverge from literature suggesting widespread forest recovery [52,132–137]. The anticipated modest growth in rubber plantations and urban areas also differs from reports of their rapid expansion in certain regions [138,139].

This divergence highlights the unique ecological dynamics and land-use pressures within GAP, emphasising the need for context-specific conservation strategies and land management policies. The specificity of the findings underscores the importance of localised environmental assessments in informing sustainable development practices, particularly in regions facing the dual challenges of preserving biodiversity while accommodating economic growth.

5. Conclusions

Tropical peatlands are vital ecosystems facing increasing pressure from anthropogenic land-use activities. Understanding how these pressures alter these ecosystems over time and projecting future changes is crucial for their sustainable management, particularly in Africa, where information on peatlands remains limited. This study presents the first attempt to analyse and predict land cover changes in the GAP from 2010 to 2020, with projections extending to 2040, using multi-source remote sensing data and machine learning techniques. The findings indicate significant land cover changes—notably, an 85% increase in rubber plantations and a 6% decrease in natural forest cover, underscoring the impact of human activities on the region. Future projections suggest minor changes in land cover by 2040. However, these projections do not account for potential impacts from climate change, large-scale development projects, and demographic shifts, which could significantly alter land cover dynamics. Continuous monitoring and adaptive management are therefore essential to ensure the resilience and sustainability of the GAP ecosystem. Overall, the research contributes to the broader understanding of land cover dynamics in tropical peatlands and emphasises the need for integrated conservation and development strategies. The methodological approach demonstrated here provides a robust framework for accurately monitoring and predicting land cover dynamics in tropical peatlands, which can be adapted for similar ecosystems globally. Policymakers and stakeholders are encouraged to utilise these insights to develop targeted actions that balance ecological preservation with socioeconomic development, ensuring long-term ecological health and human well-being in the GAP region.

Author Contributions: Conceptualization, A.O.A., P.A., P.R.-V., C.M., and I.D.-F.; methodology, A.O.A., P.A., and P.R.-V.; software, A.O.A. and P.R.-V.; validation, J.C.M., D.D.N.N., and S.K.; formal analysis, A.O.A.; investigation, A.O.A., P.A., S.K., D.D.N.N., and J.C.M.; resources, A.O.A., C.M, P.R.-V., S.K., D.D.N.N., and J.C.M.; data curation, A.O.A.; writing—original draft preparation, A.O.A.; writing—review and editing, A.O.A., P.A., P.R.-V., C.M., C.P.A., S.K., D.D.N.N., J.A.C., and J.C.M.; visualization, A.O.A.; supervision, P.A., I.D.-F., C.M., C.P.A., J.A.C., and P.R.-V.; project administration, A.O.A. and C.M. All authors have read and agreed to the published version of the manuscript.

Conflicts of Interest: Author Pedro Rodríguez-Veiga was employed by the company Sylvera Ltd. The remaining authors declare that the research was conducted in the absence of any commercial or financial relationships that could be construed as a potential conflict of interest.

References

1. FAO. *Peatland Mapping and Monitoring-Recommendations and Technical Overview*; Technical report; Food and Agriculture Organization: Rome, Italy, 2020.
2. Posa, M.R.C.; Wijedasa, L.S.; Corlett, R.T. Biodiversity and conservation of tropical peat swamp forests. *BioScience* **2011**, *61*, 49–57. [CrossRef]
3. Lhteenoja, O.; Page, S. High diversity of tropical peatland ecosystem types in the Pastaza-Maraón basin, Peruvian Amazonia. *J. Geophys. Res.* **2011**, *116*, 1–14.
4. Page, S.E.; Rieley, J.O.; Banks, C.J. Global and regional importance of the tropical peatland carbon pool. *Glob. Chang. Biol.* **2011**, *17*, 798–818. [CrossRef]
5. Leifeld, J.; Menichetti, L. The underappreciated potential of peatlands in global climate change mitigation strategies. *Nat. Commun.* **2018**, *9*, 1071. [CrossRef] [PubMed]
6. UNEP. *Global Peatlands Assessment—The State of the World's Peatlands: Evidence for Action Toward the Conservation, Restoration, and Sustainable Management of Peatlands. Main Report. Global Peatlands Initiative*; Technical report; United Nations Environment Programme: Nairobi, Kenya, 2022.
7. Paulson Insitute. *Report on Coastal Wetland Conservation Blueprint Project in China, Main Findings and Recommendations*; Technical report; Paulson Institute: Beijing, China, 2015.
8. Carless, D.; Luscombe, D.J.; Gatis, N.; Anderson, K.; Brazier, R.E. Mapping landscape-scale peatland degradation using airborne lidar and multispectral data. *Landsc. Ecol.* **2019**, *34*, 1329–1345. [CrossRef]
9. Joosten, H.; Clarke, D. *Wise Use of Mires and Peatlands*; International Mire Conservation Group and International Peat Society: Saarijärvi, Finland, 2002; Volume 304.
10. Fluet-Chouinard, E.; Stocker, B.D.; Zhang, Z.; Malhotra, A.; Melton, J.R.; Poulter, B.; Kaplan, J.O.; Goldewijk, K.K.; Siebert, S.; Minayeva, T.; et al. Extensive global wetland loss over the past three centuries. *Nature* **2023**, *614*, 281–286. [CrossRef]
11. Minasny, B.; Adetsu, D.V.; Aitkenhead, M.; Artz, R.R.; Baggaley, N.; Barthelmes, A.; Beucher, A.; Caron, J.; Conchedda, G.; Connolly, J.; et al. Mapping and monitoring peatland conditions from global to field scale. *Biogeochemistry* **2024**, *167*, 383–425. [CrossRef]
12. Page, S.; Mishra, S.; Agus, F.; Anshari, G.; Dargie, G.; Evers, S.; Jauhiainen, J.; Jaya, A.; Sancho, A.; Laurén, A.; et al. Anthropogenic impacts on lowland tropical peatland biogeochemistry. *Nat. Rev. Earth Environ.* **2022**, *3*, 426–443. [CrossRef]
13. Dargie, G.C.; Lewis, S.L.; Lawson, I.T.; Mitchard, E.T.; Page, S.E.; Bocko, Y.E.; Ifo, S.A. Age, extent and carbon storage of the central Congo Basin peatland complex. *Nature* **2017**, *542*, 86–90. [CrossRef]
14. Amoakoh, A.O.; Aplin, P.; Awuah, K.T.; Delgado-Fernandez, I.; Moses, C.; Alonso, C.P.; Kankam, S.; Mensah, C.J. Testing the contribution of multi-source remote sensing features for random forest classification of the greater amanzule tropical peatland. *Sensors* **2021**, *21*, 3399. [CrossRef]
15. Lawson, I.T.; Kelly, T.J.; Aplin, P.; Boom, A.; Dargie, G.; Draper, F.C.H.; Hassan, P.N.Z.B.P.; Hoyos-Santillan, J.; Kaduk, J.; Large, D.; et al. Improving estimates of tropical peatland area, carbon storage, and greenhouse gas fluxes. *Wetl. Ecol. Manag.* **2015**, *23*, 327–346. [CrossRef]
16. Miettinen, J.; Hooijer, A.; Shi, C.; Tollenaar, D.; Vernimmen, R.; Liew, S.C.; Malins, C.; Page, S.E. Extent of industrial plantations on S outheast A sian peatlands in 2010 with analysis of historical expansion and future projections. *Gcb Bioenergy* **2012**, *4*, 908–918. [CrossRef]
17. Crezee, B.; Dargie, G.C.; Ewango, C.E.N.; Mitchard, E.T.A.; B, O.E.; T, K.J.; Bola, P.; Ndjango, J.-B.N.; Girkin, N.T.; Bocko, Y.E.; et al. Mapping peat thickness and carbon stocks of the central Congo Basin using field data. *Nat. Geosci.* **2022**, *15*, 639–644. [CrossRef]
18. Adupong, R.; Nortey, D.D.N.; Asiedu, J. *Compilation of Customary Laws and Practices in the Greater Amanzule Wetland Areas*; Technical report; USAID Integrated Coastal and Fisheries Governance Initiative for the Western Region, Ghana; Coastal Resources Center, Graduate School of Oceanography, University of Rhode Island: Narragansett, RI, USA, 2013; pp. 1–35.
19. Kankam, S.; Inkoom, J.N.; Koo, H.; Fürst, C. Envisioning alternative futures of cultural ecosystem services supply in the coastal landscapes of Southwestern Ghana, West Africa. Socio-Ecological Practice Research. *Socio-Ecol. Pract. Res.* **2021**, *3*, 309–328. [CrossRef]
20. Hen Mpoano. *Greater Amanzule Wetland Conservation Initiative (Phase III Report)*; Technical report; Hen Mpoano and Coastal Sustainable Landscapes Project-USFS; USAID: Takoradi, Ghana, 2017.
21. Hen Mpoano. *Greater Amanzule Wetland Conservation Initiative (Phase II Report)*; Technical report; Hen Mpoano and Coastal Sustainable Landscapes Project-USFS; USAID: Takordi, Ghana, 2016.
22. Wahyunto, R.S.; Subagjo, H. *Peta Luas Sebaran Lahan Gambut dan Kandungan Karbon di Pulau Sumatera/Map of Area of Peatland Distribution and Carbon Content in Sumatera, 1990–2002*; Wetlands International—Indonesia Programme & Wildlife Habitat Canada (WHC): Jawa Barat, Indonesia, 2003.
23. Wahyunto, R.S.; Nugroho, K.; Sulaeman, Y. Indonesian peatland map: Method, certainty, and uses. In Proceedings of the Pengelolaan Berkelanjutan Lahan Gambut Terdegradasi, Jakarta, Indonesia, 6–8 October 2014; pp. 81–96.

24. Wahyunto, R.S.; Subagjo, H. *Map of Peatland Distribution Area and Carbon Content in Kalimantan*; Wetlands International—Indonesia Programme & Wildlife Habitat Canada (WHC): Jawa Barat, Indonesia, 2000.

25. Joshi, N.; Baumann, M.; Ehammer, A.; Fensholt, R.; Grogan, K.; Hostert, P.; Jepsen, M.R.; Kuemmerle, T.; Meyfroidt, P.; Mitchard, E.T.A.; et al. A review of the application of optical and radar remote sensing data fusion to land use mapping and monitoring. *Remote Sens.* **2016**, *8*, 1–23. [CrossRef]

26. Clerici, N.; Augusto, C.; Calderón, V.; Posada, J.M.; Clerici, N.; Augusto, C.; Calderón, V.; Manuel, J.; Clerici, N. Fusion of Sentinel-1A and Sentinel-2A data for land cover mapping: A case study in the lower study in the lower Magdalena region, Colombia. *J. Maps* **2017**, *13*, 718–726. [CrossRef]

27. Nomura, K.; Mitchard, E.T.A.; Patenaude, G.; Bastide, J.; Oswald, P.; Nwe, T. Oil palm concessions in southern Myanmar consist mostly of unconverted forest. *Sci. Rep.* **2019**, *9*, 11931. [CrossRef]

28. Forkuor, G.; Conrad, C.; Thiel, M.; Ullmann, T.; Zoungrana, E. Integration of optical and synthetic aperture radar imagery for improving crop mapping in northwestern Benin. *West Afr. Remote Sens.* **2014**, *6*, 6472–6499. [CrossRef]

29. Tavares, P.A.; Beltrão, N.E.S.; Guimarães, U.S.; Teodoro, C.A. Integration of sentinel-1 and sentinel-2 for classification and LULC mapping in the urban area of Belém, eastern Brazilian Amazon. *Sensors* **2019**, *19*, 1140. [CrossRef]

30. Abdi, A.M. Land cover and land use classification performance of machine learning algorithms in a boreal landscape using Sentinel-2 data. *GISci. Remote Sens.* **2020**, *57*, 1–20. [CrossRef]

31. Brown, C.; Sjögersten, S.; Ledger, M.J.; Parish, F.; Boyd, D. Remote Sensing for Restoration Change Monitoring in Tropical Peat Swamp Forests in Malaysia. *Remote Sens.* **2024**, *16*, 2690. [CrossRef]

32. Cheng, K.; Wang, J. Forest type classification based on integrated spectral-spatial-temporal features and random forest algorithm-A case study in the Qinling Mountains. *Forests* **2019**, *10*, 559. [CrossRef]

33. Habib, W.; Connolly, J. A national-scale assessment of land use change in peatlands between 1989 and 2020 using Landsat data and Google Earth Engine—A case study of Ireland. *Reg. Environ. Chang.* **2023**, *23*, 124. [CrossRef] [PubMed]

34. Ajonina, G.N.; Agardy, T.; Lau, W.; Agbogah, K.; Gormey, B. Mangrove Conditions as Indicator for Potential Payment for Ecosystem Services in Some Estuaries of Western Region of Ghana, West Africa. In *Land/Ocean Interactions in the Coastal Zone of West and Central Africa*; Diop, S., Barusseau, J.P., Descamps, C., Eds.; Springer: Cham, Switzerland, 2014; pp. 87–96.

35. Asante, W.; Jengre, N. *Carbon Stocks and Soil Nutrient Dynamics in the Peat Swamp Forests of the Amanzule Wetlands and Ankobra River Basin*; USAID Integrated Coastal and Fisheries Governance Program for the Western Region of Ghana; Nature Conservation and Research Centre: Accra, Ghana, 2012; 45p.

36. Hen Mpoano. *Fisheries Resources Inventory of Ankobra Estuary: A Step Towards Establishing Community-Based Fisheries System*; Hen Mpoano, 38 J. Cross Cole Street, Windy Ridge Extension, Takoradi; Coastal Resources Center, Graduate School of Oceanography, University of Rhode Island: Narragansett, RI, USA, 2016.

37. WD-FC. *Terrestrial ecology survey (Flora and Fauna) of the Greater Amanzule Wetland*; Hen Mpoano and Coastal Sustainable Landscapes Project: Takoradi, Ghana, 2016.

38. Xu, J.; Morris, P.J.; Liu, J.; Holden, J. PEATMAP: Refining estimates of global peatland distribution based on a meta-analysis. *Catena* **2018**, *160*, 134–140. [CrossRef]

39. Amoakoh, A.O.; Aplin, P.; Awuah, K.T.; Delgado-Fernandez, I.; Moses, C.; Alonso, C. Tropical Peatland Classification Using Multi-Sensor Sentinel Imagery and Random Forest Algorithm in Greater Amanzule, Ghana. In Proceedings of the International Geoscience and Remote Sensing Symposium (IGARSS), Athens, Greece, 7–12 July 2021; pp. 5910–5913.

40. Gorelick, N.; Hancher, M.; Dixon, M.; Ilyushchenko, S.; Thau, D.; Moore, R. Google Earth Engine: Planetary-scale geospatial analysis for everyone. *Remote Sens. Environ.* **2016**, *202*, 1–10. [CrossRef]

41. JAXA. *Global 25 m Resolution PALSAR-2/PALSAR Mosaic and Forest/Non-Forest Map (FNF); Dataset Description*; Japan Aerospace Exploration Agency (JAXA): Tsukuba, Japan, 2017.

42. Parihar, N.; Das, A.; Rathore, V.S.; Nathawat, M.S.; Mohan, S. Analysis of L-band SAR backscatter and coherence for delineation of land-use/land-cover. *Int. J. Remote Sens.* **2014**, *35*, 6781–6798. [CrossRef]

43. Shimada, M.; Ohtaki, T. Generating Large-Scale High-Quality SAR Mosaic Datasets: Application to PALSAR Data for Global Monitoring. *IEEE J. Sel. Top. Appl. Earth Obs. Remote Sens.* **2010**, *3*, 637–656. [CrossRef]

44. Hagensieker, R.; Waske, B. Evaluation of multi-frequency SAR images for tropical land cover mapping. *Remote Sens.* **2018**, *10*, 257. [CrossRef]

45. Alban, J.D.T.D.; Connette, G.M.; Oswald, P.; Webb, L.E. Combined Landsat and L-band SAR data improves land cover classification and change detection in dynamic tropical landscapes. *Remote Sens.* **2018**, *10*, 306. [CrossRef]

46. Reiche, J.; Verbesselt, J.; Hoekman, D.; Herold, M. Fusing Landsat and SAR time series to detect deforestation in the tropics. *Remote Sens. Environ.* **2015**, *156*, 276–293. [CrossRef]

47. Awuah, K.T.; Aplin, P.; Marston, C.G.; Powell, I.; Smit, I.P.J. Probabilistic mapping and spatial pattern analysis of grazing lawns in southern african savannahs using worldview-3 imagery and machine learning techniques. *Remote Sens.* **2020**, *12*, 3357. [CrossRef]

48. Corcoran, J.; Knight, J.; Pelletier, K.; Rampi, L.; Wang, Y. The effects of point or polygon-based training data on randomForest classification accuracy of wetlands. *Remote Sens.* **2015**, *7*, 4002–4025. [CrossRef]

49. Nomura, K.; Mitchard, E.T.A. More than meets the eye: Using Sentinel-2 to map small plantations in complex forest landscapes. *Remote Sens.* **2018**, *10*, 1693. [CrossRef]

50. Wang, B.; Jia, K.; Liang, S.; Xie, X.; Wei, X.; Zhao, X.; Yao, Y.; Zhang, X. Assessment of Sentinel-2 MSI spectral band reflectances for estimating fractional vegetation cover. *Remote Sens.* **2018**, *10*, 1927. [CrossRef]
51. Qiu, S.; Zhu, Z.; Olofsson, P.; Woodcock, C.E.; Jin, S. Evaluation of Landsat image compositing algorithms. *Remote Sens. Environ.* **2023**, *285*, 113375. [CrossRef]
52. Hansen, M.C.; Loveland, T.R. A review of large area monitoring of land cover change using Landsat data. *Remote Sens. Environ.* **2012**, *122*, 66–74. [CrossRef]
53. Wulder, M.A.; Masek, J.G.; Cohen, W.B.; Loveland, T.R.; Woodcock, C.E. Opening the archive: How free data has enabled the science and monitoring promise of Landsat. *Remote Sens. Environ.* **2012**, *122*, 2–10. [CrossRef]
54. Griffiths, P.; Linden, S.V.D.; Kuemmerle, T.; Hostert, P. A Pixel-Based Landsat Compositing Algorithm for Large Area Land Cover Mapping. *IEEE J. Sel. Top. Appl. Earth Obs. Remote Sens.* **2013**, *6*, 2088–2101. [CrossRef]
55. Hughes, M.; Kennedy, R. High-quality cloud masking of Landsat 8 imagery using convolutional neural networks. *Remote Sens.* **2019**, *11*, 2591. [CrossRef]
56. Qiu, S.; Lin, Y.; Shang, R.; Zhang, J.; Ma, L.; Zhu, Z. Making Landsat time series consistent: Evaluating and improving Landsat analysis ready data. *Remote Sens.* **2018**, *11*, 51. [CrossRef]
57. Lee, J.S.; Jurkevich, I.; Dewaele, P.; Wambacq, P.; Oosterlinck, A. Speckle filtering of synthetic aperture radar images: A review. *Remote Sens. Rev.* **1994**, *8*, 313–340. [CrossRef]
58. Smith, P. Bilinear interpolation of digital images. *Ultramicroscopy* **1981**, *6*, 201–204. [CrossRef]
59. Martin-Gallego, P.; Aplin, P.; Marston, C.; Altamirano, A.; Pauchard, A. Detecting and modelling alien tree presence using Sentinel-2 satellite imagery in Chile's temperate forests. *For. Ecol. Manag.* **2020**, *474*, 118353. [CrossRef]
60. Safanelli, J.L.; Poppiel, R.R.; Ruiz, L.F.C.; Bonfatti, B.R.; Oliveira, D.; Mello, F.A.; Rizzo, R.; Demattê, M.J.A. Terrain analysis in Google Earth Engine: A method adapted for high-performance global-scale analysis. *ISPRS Int. J. Geo-Inf.* **2020**, *9*, 400. [CrossRef]
61. Guyon, I.; Elisseeff, A. An Introduction to Variable and Feature Selection. *J. Mach. Learn. Res.* **2003**, *3*, 1157–1182.
62. Pedregosa, F.; Varoquaux, G.; Gramfort, A.; Michel, V.; Thirion, B.; Grisel, O.; Blondel, M.; Prettenhofer, P.; Weiss, R.; Dubourg, V.; et al. Scikit-learn: Machine Learning in Python. *J. Mach. Learn. Res.* **2011**, *39*, 2826–2830.
63. Belgiu, M.; Drăguţ, L. Random forest in remote sensing: A review of applications and future directions. *ISPRS J. Photogramm. Remote Sens.* **2016**, *114*, 24–31. [CrossRef]
64. Waske, B.; Braun, M. Classifier ensembles for land cover mapping using multitemporal SAR imagery. *ISPRS J. Photogramm. Remote Sens.* **2009**, *64*, 450–457. [CrossRef]
65. Kaszta, Z.; Kerchove, R.V.D.; Ramoelo, A.; Cho, M.A.; Madonsela, S.; Mathieu, R.; Wolff, E. Seasonal separation of African savanna components using WorldView-2 imagery: A comparison of pixeland object-based approaches and selected classification algorithms. *Remote Sens.* **2016**, *8*, 763. [CrossRef]
66. Breiman, L.; Friedman, J.; Stone, C.J.; Olshen, A.R. *Classification and Regression Trees. First*; Chapman and Hall/CRC: Belmont, CA, USA, 1984.
67. Quinlan, J.R. *C4.5 Programs for Machine Learning*; Morgan Kaurmann: San Mateo, CA, USA, 1993.
68. Mingers, J. An empirical comparison of selection measures for decision-tree induction. *Mach. Learn.* **1989**, *3*, 319–342. [CrossRef]
69. Rodriguez-Galiano, V.F.; Ghimire, B.; Rogan, J.; Chica-Olmo, M.; Rigol-Sanchez, J.P. An assessment of the effectiveness of a random forest classifier for land-cover classification. *ISPRS J. Photogramm. Remote Sens.* **2012**, *67*, 93–104. [CrossRef]
70. Congalton, R.G. Accuracy assessment and validation of remotely sensed and other spatial information. *Int. J. Wildland Fire* **2001**, *10*, 321–328. [CrossRef]
71. Olofsson, P.; Foody, G.M.; Herold, M.; Stehman, S.V.; Woodcock, C.E.; Wulder, M.A. Good practices for estimating area and assessing accuracy of land change. *Remote Sens. Environ.* **2014**, *148*, 42–57. [CrossRef]
72. Guidigan, M.L.G.; Sanou, C.L.; Ragatoa, D.S.; Fafa, C.O.; Mishra, N.V. Assessing Land Use/Land Cover Dynamic and Its Impact in Benin Republic Using Land Change Model and CCI-LC Products. *Earth Syst. Environ.* **2019**, *3*, 127–137. [CrossRef]
73. Aneesha Satya, B.; Shashi, M.; Deva, P. Future land use land cover scenario simulation using open-source GIS for the city of Warangal, Telangana, India. *Appl. Geomat.* **2020**, *12*, 281–290. [CrossRef]
74. Baig, M.F.; Mustafa, M.R.U.; Baig, I.; Takaijudin, H.B.; Zeshan, T.M. Assessment of Land Use Land Cover Changes and Future Predictions Using CA-ANN Simulation for Selangor, Malaysia. *Water* **2022**, *14*, 402. [CrossRef]
75. Losiri, C.; Nagai, M.; Ninsawat, S.; Shrestha, P.R. Modeling urban expansion in Bangkok Metropolitan region using demographic-economic data through cellular Automata-Markov Chain and Multi-Layer Perceptron-Markov Chain models. *Sustainability* **2016**, *8*, 686. [CrossRef]
76. Kamaraj, M.; Rangarajan, S. Predicting the future land use and land cover changes for Bhavani basin, Tamil Nadu, India, using QGIS MOLUSCE plugin. *Environ. Sci. Pollut. Res.* **2022**, *29*, 86337–86348. [CrossRef]
77. Kafy, A.A.; Rahman, M.S.; Faisal, A.A.; Hasan, M.M.; Islam, M. Modelling future land use land cover changes and their impacts on land surface temperatures in Rajshahi, Bangladesh. *Remote Sens. Appl. Soc. Environ.* **2020**, *18*, 100314. [CrossRef]
78. De'Smith, M.J.; Goodchild, M.F.; Longley, P. *Geospatial Analysis: A Comprehensive Guide to Principles, Techniques and Software Tools*, 6th ed.; Spatial Analysis Online: London, UK, 2018.
79. Ullah, S.; Tahir, A.A.; Akbar, T.A.; Hassan, Q.K.; Dewan, A.; Khan, A.J.; Khan, M. Remote sensing-based quantification of the relationships between land use land cover changes and surface temperature over the lower Himalayan region. *Sustainability* **2019**, *11*, 5492. [CrossRef]

80. Alawamy, J.S.; Balasundram, S.K.; Hanif, A.H.M.; Sung, C.T.B. Detecting and analyzing land use and land cover changes in the Region of Al-Jabal Al-Akhdar, Libya using time-series Landsat data from 1985 to 2017. *Sustainability* **2017**, *12*, 4490. [CrossRef]

81. Li, Y.; Zhao, Q.; Zhong, C. GIS and urban data science. *Ann. GIS* **2022**, *28*, 89–92. [CrossRef]

82. Su, S.; Xiao, R.; Zhang, Y. Multi-scale analysis of spatially varying relationships between agricultural landscape patterns and urbanization using geographically weighted regression. *Appl. Geogr.* **2012**, *32*, 360–375. [CrossRef]

83. Pontius, G.R.; Malanson, J. Comparison of the structure and accuracy of two land change models. *Int. J. Geogr. Inf. Sci.* **2005**, *19*, 243–265. [CrossRef]

84. Verburg, P.H.; Crossman, N.; Ellis, E.C.; Heinimann, A.; Hostert, P.; Mertz, O.; Nagendra, H.; Sikor, T.; Erb, K.H.; Golubiewski, N.; et al. Land system science and sustainable development of the earth system: A global land project perspective. *Anthropocene* **2015**, *12*, 29–41. [CrossRef]

85. D'oleire-Oltmanns, S.; Coenradie, S.; Kleinschmit, B. An object-based classification approach for mapping migrant housing in the mega-urban area of the Pearl River Delta (China). *Remote Sens.* **2011**, *3*, 1710–1723. [CrossRef]

86. Lidzhegu, Z.; Ellery, W.N.; Mantel, S.K.; Hughes, D.A. Delineating wetland areas from the cut-and-fill method using a Digital Elevation Model (DEM). *S. Afr. Geogr. J.* **2020**, *102*, 97–115. [CrossRef]

87. Balzter, H.; Cole, B.; Thiel, C.; Schmullius, C. Mapping CORINE Land Cover from Sentinel-1A SAR and SRTM Digital Elevation Model Data using Random Forests. *Remote Sens.* **2014**, *7*, 14876–14898. [CrossRef]

88. Soria-Ruiz, J.; Fernandez-Ordoñez, Y.; Woodhouse, H.I. Land-cover classification using radar and optical images: A case study in Central Mexico. *Int. J. Remote Sens.* **2010**, *31*, 3291–3305. [CrossRef]

89. Frampton, W.J.; Dash, J.; Watmough, G.; Milton, E.J. Evaluating the capabilities of Sentinel-2 for quantitative estimation of biophysical variables in vegetation. *ISPRS J. Photogramm. Remote Sens.* **2013**, *82*, 83–92. [CrossRef]

90. Rajah, P.; Odindi, J.; Mutanga, O.; Kiala, Z. The utility of Sentinel-2 Vegetation Indices (VIs) and Sentinel-1 Synthetic Aperture Radar (SAR) for invasive alien species detection and mapping. *Nat. Conserv.* **2019**, *35*, 41–61. [CrossRef]

91. Novando, G.; Arif, D.A.; D, P.S. Comparison of soil adjusted vegetation index (SAVI) and modified soil adjusted vegetation index (MSAVI) methods to view vegetation density in Padang city using LANSAT 8 image. *Int. Remote Sens. Appl. J.* **2021**, *2*, 31–36. [CrossRef]

92. Allbed, A.; Kumar, L.; Sinha, P. Mapping and modelling spatial variation in soil salinity in the Al Hassa Oasis based on remote sensing indicators and regression techniques. *Remote Sens.* **2014**, *6*, 1137–1157. [CrossRef]

93. Khatami, R.; Mountrakis, G.; Stehman, S.V. A meta-analysis of remote sensing research on supervised pixel-based land-cover image classification processes: General guidelines for practitioners and future research. *Remote Sens. Environ.* **2016**, *177*, 89–100. [CrossRef]

94. Pu, R.; Landry, S.; Yu, Q. Assessing the potential of multi-seasonal high resolution Pléiades satellite imagery for mapping urban tree species. *Int. J. Appl. Earth Obs. Geoinf.* **2018**, *71*, 144–158.

95. Haralick, R.M.; Dinstein, I.; Shanmugam, K. Textural Features for Image Classification. *IEEE Trans. Syst. Man Cybern. SMC* **1973**, *3*, 610–621. [CrossRef]

96. Johansen, K.; Phinn, S. Mapping structural parameters and species composition of riparian vegetation using Ikonos and Landsat ETM+ data in Australian tropical savannahs. *Photogramm. Eng. Remote Sens.* **2006**, *72*, 71–80. [CrossRef]

97. Hansen, M.C.; Potapov, P.V.; Moore, R.; Hancher, M.; Turubanova, S.A.; Tyukavina, A.; Thau, D.; Stehman, S.V.; Goetz, S.J.; Loveland, T.R.; et al. High-resolution global maps of 21st-century forest cover change. *Science* **2013**, *342*, 850–853. [CrossRef]

98. Griffiths, P.; Kuemmerle, T.; Baumann, M.; Radeloff, V.C.; Abrudan, I.V.; Lieskovsky, J.; Munteanu, C.; Ostapowicz, K.; Hostert, P. Forest disturbances, forest recovery, and changes in forest types across the Carpathian ecoregion from 1985 to 2010 based on Landsat image composites. *Remote Sens. Environ.* **2014**, *151*, 72–88; Special Issue on 2012 ForestSAT. [CrossRef]

99. Lopes, M.; Frison, P.L.; Crowson, M.; Warren-Thomas, E.; Hariyadi, B.; Kartika, W.D.; Agus, F.; Hamer, K.C.; Stringer, L.; Hill, J.K.; et al. Improving the accuracy of land cover classification in cloud persistent areas using optical and radar satellite image time series. *Methods Ecol. Evol.* **2020**, *11*, 532–541. [CrossRef]

100. Heumann, B.W. Satellite remote sensing of mangrove forests: Recent advances and future opportunities. *Prog. Phys. Geogr.* **2011**, *35*, 87–108. [CrossRef]

101. Kuenzer, C.; Bluemel, A.; Gebhardt, S.; Quoc, T.V.; Dech, S. Remote sensing of mangrove ecosystems: A review. *Remote Sens.* **2011**, *3*, 878–928. [CrossRef]

102. Gumbricht, T.; Roman-Cuesta, R.M.; Verchot, L.; Herold, M.; Wittmann, F.; Householder, E.; Herold, N.; Murdiyarso, D. An expert system model for mapping tropical wetlands and peatlands reveals South America as the largest contributor. *Glob. Chang. Biol.* **2017**, *23*, 3581–3599. [CrossRef] [PubMed]

103. Miettinen, J.; Hooijer, A.; Vernimmen, R.; Liew, S.C.; Page, E.S. From carbon sink to carbon source: Extensive peat oxidation in insular Southeast Asia since 1990. *Environ. Res. Lett.* **2017**, *12*, 024014. [CrossRef]

104. Charters, L.J.; Aplin, P.; Marston, C.G.; Padfield, R.; Rengasamy, N.; Bin Dahalan, M.P.; Evers, S. Peat swamp forest conservation withstands pervasive land conversion to oil palm plantation in North Selangor, Malaysia. *Int. J. Remote Sens.* **2019**, *40*, 7409–7438. [CrossRef]

105. Gong, P.; Wang, J.; Yu, L.; Zhao, Y.; Zhao, Y.; Liang, L.; Niu, Z.; Huang, X.; Fu, H.; Liu, S.; et al. Finer resolution observation and monitoring of global land cover: First mapping results with Landsat TM and ETM+ data. *Int. J. Remote Sens.* **2013**, *34*, 2607–2654. [CrossRef]

106. Lu, D.; Weng, Q. A survey of image classification methods and techniques for improving classification performance. *Int. J. Remote Sens.* **2007**, *28*, 823–870. [CrossRef]

107. Dargie, G.C.; Lawson, I.T.; Rayden, T.J.; Miles, L.; Mitchard, E.T.A.; Page, S.E.; Bocko, Y.E.; Ifo, S.A.; Lewis, L.S. Congo Basin peatlands: Threats and conservation priorities. *Mitig. Adapt. Strateg. Glob. Chang.* **2019**, *24*, 669–686. [CrossRef]

108. Ung, V. Review of the book biotic evolution and environmental change in Southeast Asia - Edited by David Gower, Kenneth Johnson, James Richardson, Brian Rosen, Lukas Rüber, and Suzanne Williams. *Syst. Biol.* **2013**, *62*, 913–915. [CrossRef]

109. Roucoux, K.H.; Lawson, I.T.; Baker, T.R.; Torres, D.D.C.; Draper, F.C.; Lähteenoja, O.; Gilmore, M.P.; Honorio Coronado, E.N.; Kelly, T.J.; Mitchard, E.T.A.; et al. Threats to intact tropical peatlands and opportunities for their conservation. *Conserv. Biol.* **2017**, *31*, 1283–1292. [CrossRef]

110. Dommain, R.; Couwenberg, J.; Glaser, P.H.; Joosten, H.; Suryadiputra, N.I.N. Carbon storage and release in Indonesian peatlands since the last deglaciation. *Quat. Sci. Rev.* **2014**, *97*, 1–31. [CrossRef]

111. Ziegler, A.D.; Fox, J.M.; Xu, J. The rubber juggernauts. *Science* **2009**, *324*, 1024–1025. [CrossRef] [PubMed]

112. Ahrends, A.; Hollingsworth, P.M.; Ziegler, A.D.; Fox, J.M.; Chen, H.; Su, Y.; Xu, J. Current trends of rubber plantation expansion may threaten biodiversity and livelihoods. *Glob. Environ. Chang.* **2015**, *34*, 48–58. [CrossRef]

113. Neyret, M.; Robain, H.; De Rouw, A.; Soulileuth, B.; Trisophon, K.; Jumpa, K.; Valentin, C. The transition from arable lands to rubber tree plantations in northern Thailand impacts weed assemblages and soil physical properties. *Soil Use Manag.* **2018**, *34*, 404–417. [CrossRef]

114. Ruf, F.O. *Ecological Factors Influencing Crop Diversification in the Axim Region of Ghana: From Coconut to Cocoa*; CIRAD-Forêt: Montpellier, France, 2005.

115. Nkansah-Poku, J.; Philippe, R.; Quaicoe, R.N.; Dery, S.K.; Ransford, A. Cape Saint Paul Wilt disease of coconut in Ghana: Surveillance and management of disease spread. *Agron.-Environ.* **2009**, *16*, 111–115. [CrossRef]

116. Okorley, E.; Haizel, E. Farmers' Attitudes and Problems Associated with The Adoption Of Cape Saint Paul Resistant Coconut Hybrid In The Western Region Of Ghana. *Agron. Afr.* **2009**, *16*, 83–89. [CrossRef]

117. Quaiku, W. Assessing the Economic Effects of Cape Saint Paul' s Wilt Coconut Disease on the People of Nzema East District. *J. Educ. Pract.* **2013**, *4*, 66–71.

118. Nredah, I.A. Comparing the Alternative Utilization Method for Coconut in Nzema. Master's Thesis, Lappeenranta University of Technology, Lappeenranta, Finland, 2015.

119. GSS. *Ghana 2021 Population and Housing Census*; General Report Volume 3A; Ghana Statistical Service: Accra, Ghana, 2021; pp. 1–111.

120. Bullock, C.H.; Collier, M.J.; Convery, F. Peatlands, their economic value and priorities for their future management—The example of Ireland. *Land Use Policy* **2012**, *29*, 921–928. [CrossRef]

121. Gibson, J.J.; Eby, P.; Birks, S.J.; Twitchell, C.; Gray, C.; Kariyeva, J. Isotope-based water balance assessment of open water wetlands across Alberta: Regional trends with emphasis on the oil sands region. *J. Hydrol. Reg. Stud.* **2022**, *40*, 1–18. [CrossRef]

122. Rieley, J.O. Biodiversity of Tropical Peatland in Southeast Asia. In Proceedings of the 15th International Peat Congress, Kuching, Sarawak, Malaysia, 15–19 August 2016; pp. 707–711.

123. Yule, C.M. Loss of biodiversity and ecosystem functioning in Indo-Malayan peat swamp forests. *Biodivers. Conserv.* **2010**, *19*, 393–409. [CrossRef]

124. Beukema, H.; Danielsen, F.; Vincent, G.; Hardiwinoto, S.; Andel, J.V. Plant and bird diversity in rubber agroforests in the lowlands of Sumatra, Indonesia. *Agrofor. Syst.* **2007**, *70*, 217–242. [CrossRef]

125. Dong, J.; Xiao, X.; Sheldon, S.; Biradar, C.; Xie, G. Mapping tropical forests and rubber plantations in complex landscapes by integrating PALSAR and MODIS imagery. *ISPRS J. Photogramm. Remote Sens.* **2012**, *74*, 20–33. [CrossRef]

126. Deng, J.S.; Wang, K.; Hong, Y.; Qi, J.G. Spatio-temporal dynamics and evolution of land use change and landscape pattern in response to rapid urbanization. *Landsc. Urban Plan.* **2009**, *92*, 187–198. [CrossRef]

127. Acheampong, E.; Insaidoo, T.F.G.; Ros-Tonen, F.M.A. Management of Ghana's modified taungya system: Challenges and strategies for improvement. *Agrofor. Syst.* **2016**, *90*, 659–674. [CrossRef]

128. Samsudin, Y.B.; Puspitaloka, D.; Rahman, S.A.; Chandran, A.; Baral, H. Community-Based Peat Swamp Restoration Through Agroforestry in Indonesia. *Agrofor. Degrad. Landsc.* **2020**, *1*, 349–365.

129. Loisel, J.; Gallego-Sala, A. Ecological resilience of restored peatlands to climate change. *Commun. Earth Environ.* **2022**, *3*, 208. [CrossRef]

130. Turner, M.G. Landscape ecology: What is the state of the science? *Evol. Syst.* **2005**, *36*, 319–344. [CrossRef]

131. PHDC. *Republic of Ghana Investment Guide*; Petroleum Hub Development Cooperation: Accra, Ghana, 2022.

132. Curtis, P.G.; Slay, C.M.; Harris, N.L.; Tyukavina, A.; Hansen, M.C. Classifying drivers of global forest loss. *Science* **2018**, *361*, 1108–1111. [CrossRef]

133. Richards, D.R.; Thompson, B.S.; Wijedasa, L. Quantifying net loss of global mangrove carbon stocks from 20 years of land cover change. *Nat. Commun.* **2020**, *11*, 4260. [CrossRef]

134. Goldberg, L.; Lagomasino, D.; Thomas, N.; Fatoyinbo, T. Global declines in human-driven mangrove loss. *Glob. Chang. Biol.* **2020**, *26*, 5844–5855. [CrossRef]

135. Hagger, V.; Worthington, T.A.; Lovelock, C.E.; Adame, M.F.; Amano, T.; Brown, B.M.; Friess, D.A.; Landis, E.; Mumby, P.J.; Morrison, T.H.; et al. Drivers of global mangrove loss and gain in social-ecological systems. *Nat. Commun.* **2022**, *13*, 6373. [CrossRef] [PubMed]

136. Bunting, P.; Rosenqvist, A.; Hilarides, L.; Lucas, R.M.; Thomas, N.; Tadono, T.; Worthington, T.A.; Spalding, M.; Murray, N.J.; Rebelo, L.-M. Global Mangrove Extent Change 1996–2020: Global Mangrove Watch Version 3.0. *Remote Sens.* **2022**, *14*, 3657. [CrossRef]

137. Thomas, N.; Lucas, R.; Bunting, P.; Hardy, A.; Rosenqvist, A.; Simard, M. Distribution and drivers of global mangrove forest change. *PLoS ONE* **2017**, *12*, e0179302. [CrossRef] [PubMed]

138. Li, Z.; Fox, J.M. Mapping rubber tree growth in mainland Southeast Asia using time-series MODIS 250 m NDVI and statistical data. *Appl. Geogr.* **2012**, *32*, 420–432. [CrossRef]

139. Seto, K.C.; Güneralp, B.; Hutyra, R.L. Global forecasts of urban expansion to 2030 and direct impacts on biodiversity and carbon pools. *Proc. Natl. Acad. Sci. USA* **2012**, *109*, 16083–16088. [CrossRef]